American Mineralogist, Volume 105, pages 1490–1507, 2020

Mineral compositions and thermobarometry of basalts and boninites recovered during IODP Expedition 352 to the Bonin forearc

Scott A. Whattam[1,*,†], John W. Shervais[2], Mark K. Reagan[3], Daniel A. Coulthard Jr.[3,4], Julian A. Pearce[5], Peter Jones[6], Jieun Seo[7], Keith Putirka[8], Timothy Chapman[9,10], Daniel Heaton[11], Hongyan Li[12], Wendy R. Nelson[13], Kenji Shimizu[14], and Robert J. Stern[15]

[1]Department of Geosciences, King Fahd University of Petroleum and Minerals, Dhahran 31261, Saudi Arabia
[2]Department of Geology, Utah State University, Logan, Utah 84322-4505, U.S.A.
[3]Department of Earth and Environmental Sciences, University of Iowa, Iowa City, Iowa 52242, U.S.A.
[4]Volcanic Risk Solutions, Massey University, Palmerston North 4414, New Zealand
[5]School of Earth, Ocean and Planetary Sciences, Cardiff University, Cardiff CF10 3YE, U.K.
[6]Department of Earth Sciences, Carleton University, Ottawa, Ontario K1S 5B6, Canada
[7]Department of Earth and Environmental Sciences, Korea University, Seoul 02841, South Korea
[8]Department of Earth and Environmental Sciences, California State University, Fresno, California 93740, U.S.A.
[9]School of Geosciences, University of Sydney, New South Wales 2006, Australia
[10]Earth Science, School of Environmental and Rural Science, University of New England, New South Wales 2351, Australia
[11]College of Earth, Ocean and Atmospheric Sciences, Oregon State University, Corvalis, Oregon 97331-5503, U.S.A.
[12]State Key Laboratory of Isotope Geochemistry, Guangzhou Institute of Geochemistry, Chinese Academy of Sciences, Guangzhou 510640, PR China
[13]Department of Physics, Astronomy and Geosciences, Towson University, Towson, Maryland 21252, U.S.A.
[14]Kochi Institute for Core Sample Research, Japan Agency for Marine-Earth Science and Technology, Monobe-otsu 200, Nankoku, Kochi, 783-8502, Japan
[15]Geosciences Department, University of Texas at Dallas, Richardson, Texas 75083-0688, U.S.A.

Abstract

Central aims of IODP Expedition 352 were to delineate and characterize the magmatic stratigraphy in the Bonin forearc to define key magmatic processes associated with subduction initiation and their potential links to ophiolites. Expedition 352 penetrated 1.2 km of magmatic basement at four sites and recovered three principal lithologies: tholeiitic forearc basalt (FAB), high-Mg andesite, and boninite, with subordinate andesite. Boninites are subdivided into basaltic, low-Si, and high-Si varieties. The purpose of this study is to determine conditions of crystal growth and differentiation for Expedition 352 lavas and compare and contrast these conditions with those recorded in lavas from mid-ocean ridges, forearcs, and ophiolites. Cr# (cationic Cr/Cr+Al) vs. TiO_2 relations in spinel and clinopyroxene demonstrate a trend of source depletion with time for the Expedition 352 forearc basalt to boninite sequence that is similar to sequences in the Oman and other suprasubduction zone ophiolites. Clinopyroxene thermobarometry results indicate that FAB crystallized at temperatures (1142–1190 °C) within the range of MORB (1133–1240 °C). When taking into consideration liquid lines of descent of boninite, orthopyroxene barometry and olivine thermometry of Expedition 352 boninites demonstrate that they crystallized at temperatures marginally lower than those of FAB, between ~1119 and ~1202 °C and at relatively lower pressure (~0.2–0.4 vs. 0.5–4.6 kbar for FAB). Elevated temperatures of boninite orthopyroxene (~1214 °C for low-Si boninite and 1231–1264 °C for high-Si boninite) may suggest latent heat produced by the rapid crystallization of orthopyroxene. The lower pressure of crystallization of the boninite may be explained by their lower density and hence higher ascent rate, and shorter distance of travel from place of magma formation to site of crystallization, which allowed the more buoyant and faster ascending boninites to rise to shallower levels before crystallizing, thus preserving their high temperatures.

Keywords: International Ocean Discovery Program (IODP), JOIDES Resolution, Expedition 352, Izu-Bonin-Mariana Fore Arc, forearc basalt, boninite, ophiolite, Sites U1439, U1440, U1441, U1442; New Advances in Subduction Zone Magma Genesis

Introduction

A strong genetic link between ophiolites and intra-oceanic arc systems has been recognized for some time (Miyashiro 1973; Alabaster et al. 1982), and a more specific linkage with subduction initiation has been made more recently (Stern and Bloomer 1992; Shervais 2001; Pearce and Robinson 2010; Whattam and Stern 2011; Stern et al. 2012; Moghadam et al. 2014). Nonetheless, controversy as to whether ophiolites mostly form in magmatic arcs or at mid-ocean ridges has persisted because, from a chemical and structural point of view, some ophiolites have chemical compositions like those of mid-ocean ridge basalt (MORB) while many others have chemical compositions like

* E-mail: sawhatta@gmail.com
† Special collection papers can be found online at http://www.minsocam.org/MSA/AmMin/special-collections.html.

0003-004X/20/0010–1490$05.00/DOI: https://doi.org/10.2138/am-2020-6640

those of arcs. Part of this confusion lies in the fact that many ophiolites contain both a MORB-like unit and a volcanic arc-like unit, which suggests formation of each suite in two distinct tectonic environments. The early identification of the MORB-like component led to the interpretation that ophiolites are obducted remnants of normal oceanic lithosphere, like those produced today at the Mid-Atlantic Ridge or East Pacific Rise (e.g., Coleman 1981; Moores 1982), but further study has consistently identified an arc-like chemical signature in most ophiolites (see Metcalf and Shervais 2008 for a review of the "ophiolite conundrum"). The recognition of MORB- and arc-like magmas has led to the interpretation that ophiolites represent fragments of oceanic lithosphere generated in supra-subduction zone settings (Miyashiro 1973; Pearce et al. 1984; Pearce 2003; Saccani and Photiades 2004; Dilek et al. 2007, 2008; Moghadam and Stern 2014) with many studies suggesting formation within back arc basins (e.g., Evans et al. 1991; Monnier et al. 1995; Thompson et al. 1997; Cluzel et al. 2001; Saccani et al. 2008), to reconcile the chemical bimodality. Models entailing formation above a reconfigured subduction zone subsequent to a major tectonic reorganization and establishment of a new subduction zone within the original mid-ocean ridge or back arc were also advanced (see review of Whattam 2009).

A key breakthrough in reconciling these perspectives was the discovery that the most abundant lavas cropping out on the Mariana (Reagan et al. 2010, 2013), Izu (DeBari et al. 1999), and Bonin (Ishizuka et al. 2011) forearc trench slopes were MORB-like tholeiites termed "forearc basalts" (or "FAB" ; Reagan et al. 2010). These FAB are older than boninites exposed upslope in the forearc (cf. Ishizuka et al. 2006, 2011; Reagan et al. 2019), suggesting that seafloor spreading occurred immediately after subduction initiation to generate FAB and that boninites were generated later after fluids from the subducting slab became involved in magma genesis (Reagan et al. 2017). In an effort to extend these insights from marine geology on land, the subduction initiation rule of Whattam and Stern (2011) hypothesizes that all magmatic components (i.e., MORB, arc basalt, and boninite) of most well-preserved ophiolites form in similar proto-forearc settings and follow a predictable chemotemporal progression as a new subduction zone forms. This model is consistent with the hypothesis that seafloor spreading in a proto-forearc environment accompanies subduction initiation (Shervais 2001; Stern et al. 2012).

The motivating force behind IODP Expedition 352, which drilled into the outer Bonin forearc, was to test the aforementioned models. Here, we analyze the compositions of minerals from Expedition 352 lavas to determine the conditions of crystal growth and differentiation. We then compare and contrast the mineral compositions and thermobarometry with those of MORB and ophiolites, specifically testing the hypothesis that ophiolites are more closely linked to subduction initiation rather than to regular ocean basin seafloor spreading.

Geologic and tectonic background

The Izu-Bonin-Mariana (IBM) intra-oceanic arc stretches 2800 km from the Izu peninsula, Japan, to seamounts west of Guam, U.S.A. (Fig. 1). The IBM represents one of the most intensely studied intra-oceanic arcs on Earth, as numerous drilling expeditions, including IODP Expedition 352, manned submersible dives, and dredging cruises on and along the forearc have targeted this archtypical geologic setting (e.g., Bloomer and Hawkins 1983; Ishizuka et al. 2006, 2011; Reagan et al. 2010, 2013, 2015, 2017). Some suggest that the IBM subduction zone began due to hemispheric-scale foundering of old, dense lithosphere comprising the western segment of the Pacific Plate and its ultimate subduction to the west beneath the Philippine Sea Plate (Stern and Bloomer 1992; Bloomer et al. 1995; Stern et al. 2012). Leng and Gurnis (2015) however, propose an alternative model entailing the combination of thermal and compositional density contrasts between the overriding relic arc and adjacent old Pacific oceanic plate, the conditions of which promoted spontaneous subduction initiation (see also Stern and Bloomer 1992; Niu et al. 2003). A third model postulates that subduction was nucleated above the Manus plume (0°N/150°E) near the Pacific-East Asian Sea plate boundary circa in the middle Eocene (Macpherson and Hall 2001; Wu et al. 2016). Large-scale formation of seafloor crust in the IBM forearc after subduction initiation began between 52.5 and 51.9 Ma (Ishizuka et al. 2011; Reagan et al. 2013, 2019). The Philippine Sea plate subsequently migrated northward and was accompanied by post-40 Ma maximum 80° clockwise rotation. The predominantly submarine convergent plate boundary is thus the result of ~52 My of subduction of the Pacific Plate beneath the eastern margin of the Philippine Sea Plate.

The sequence of initial magmatic products preserved in the IBM forearc is "ophiolite-like" and is similar everywhere the forearc has been sampled (Bloomer and Hawkins 1983; Stern and Bloomer 1992; DeBari et al. 1999; Reagan et al. 2010, 2013, 2017; Ishizuka et al. 2011). This commonality implies that a short (<1 Ma), but intense episode of asthenospheric upwelling, magmatism, and seafloor spreading to generate FAB-related crust occurred immediately after subduction initiation (Reagan et al. 2019). This zone of upwelling, melting, and magmatism occurred over tens to hundreds of kilometers across the entire arc (Arculus et al. 2015; Hickey-Vargas et al. 2018; Yogodzinski et al. 2018). Boninite volcanism followed closely after FAB formation, beginning at ca. 51.3 Ma and lasting through to ca. 46 Ma (Ishizuka et al. 2006, 2011; Reagan et al. 2019).

The presence of boninites is in itself an important tectonic indicator. Numerous petrological, geochemical, and experimental studies (e.g., Crawford et al. 1989; Umino and Kushiro 1989; van der Laan et al. 1989; Pearce et al. 1992; Taylor et al. 1994; Kushiro 1972, 1974; Green 1973, 1976; Mitchell and Grove 2015) have suggested that boninite magmas are generated via high degrees of partial melting (of the order of >20%) of refractory mantle fluxed with slab-derived fluids or melts in subduction environments with modest temperatures (~1130–1275 °C) and low pressure (0.3–1.7 kbar; see reviews by Kushiro 2007; Pearce and Reagan 2019).

Subsequent to boninite production in the IBM forearc, igneous activity retreated westward toward where the magmatic arc is today. This later activity was characterized by the production of normal arc tholeiitic and calc-alkaline magmas beginning at ca. 45 Ma, thereby marking the establishment of a mature and stable magmatic arc system (Ishizuka et al. 2006, 2011; Reagan et al. 2019).

Study area

IODP Expedition 352 drilled the northern IBM forearc to the immediate northeast of the Bonin Islands between 142°30′E

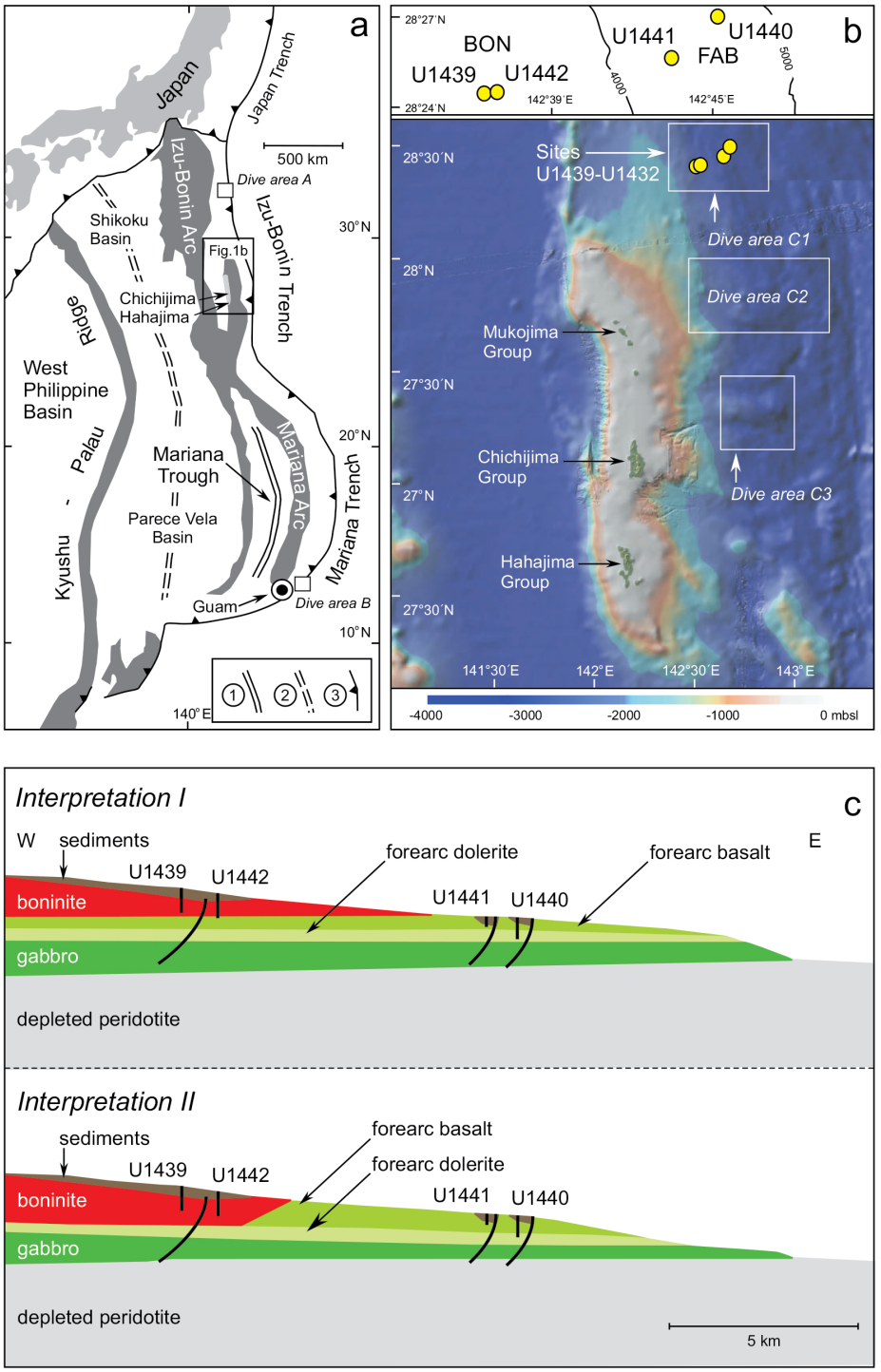

Figure 1. Study areas. (**a**) Geological setting of the Izu-Bonin Mariana arc system in the western Pacific. The circled numbers 1, 2, and 3 represent active spreading ridges, extinct spreading ridges and convergent margin or trenches (i.e., subduction zones), respectively; the boxes labeled "Dive area A" and "Dive area B" to the immediate east of the Izu-Bonin Arc and Guam represent the regions in which the dive sites of DeBari et al. (1999) and Reagan et al. (2010), respectively, were conducted as discussed in the text. (**b**) Location of Expedition 352 drill sites to the immediate NE of the Bonin Islands. Box above, magnification of Sites U1439, U1442, U1440, and U1441 (filled yellow circles) shown in main figure. The boxes labeled "Dive area C1, C2, and C3" represent the dive sites of Ishizuka et al. (2011) as discussed in the text. (**c**) Two alternative interpretations of the stratigraphic section (not to scale) of the Bonin forearc drill site area. Interpretation I (top) entails FAB underlying boninite whereas the second one (bottom) entails FAB lying "trenchward" and the boninite lying "arcward." The bottom panel (second interpretation) is from Reagan et al. (2015). (Color online.)

and 143°00′E and 28°24′N and 28°27′N (Reagan et al. 2015) (Fig. 1b). Four drill sites were cored: U1440 and U1441 are closest to the trench and U1439 and U1442 are upslope and to the west (Fig. 1c). Sites U1440 and U1441 recovered FAB and related hypabyssal rocks (dolerite dikes, Reagan et al. 2017; Shervais et al. 2019), whereas boninite series and high-Mg andesite lavas were recovered from Sites U1439 and U1442. A total of 1.22 km of magmatic basement was cored.

Expedition 352 results suggest FAB erupted shortly after subduction initiation and were generated by seafloor spreading, as shown by the widespread presence of mafic dikes, with little to no subduction input and compositions similar to those of the most depleted MORB (Reagan et al. 2017; Shervais, et al. 2019). Subsequent to extraction of FAB, continued melting of a more depleted mantle caused by fluxing of subduction components is inferred to result in the generation of the boninites. This succession is analogous to that recorded by many ophiolites, thus providing a direct link between subduction initiation, forearc spreading and ophiolite genesis (Stern and Bloomer 1992; Shervais 2001; Reagan et al. 2010, 2017; Whattam and Stern 2011; Stern et al. 2012)

Methods

Electron probe micro-analyzer

Approximately 70 samples of tholeiitic FAB, high-Mg andesite, boninite, and subordinate andesite were chosen for electron probe micro-analyzer (EPMA) analysis. Quantitative analyses were made on an automated 4 spectrometer Cameca Camebax MBX electron probe housed in the Department of Earth Sciences, Carleton University (Ottawa, Canada) by the wavelength-dispersive X-ray analysis method (WDX). Operating conditions involved a 20 kV accelerating potential and a beam current of 20 nA. Beam sensitive minerals such as feldspar, were analyzed using a rastered electron beam of ~8 × 8 µm in size and a focused beam size of 1 µm was used for microlites of clinopyroxene and feldspar. Alkali elements such as Na and K were analyzed first. Peak counting times were ca. 15–20 s, unless X-ray counts exceeded 40 000. Background positions were chosen carefully to avoid interferences from adjacent peaks and measurements were made at 50% of the peak counting time. Raw X-ray data were converted to elemental wt% by the Cameca PAP matrix correction program. A suite of well-characterized natural and synthetic minerals and compounds were used as primary and secondary calibration standards. Kakanui kaersutite K1 and USNM Kakanui hornblende and USNM chromium augite (Reay el al. 1989; Jarosewich et al. 1980) were analyzed as internal standards to monitor data quality. Analyses are accurate to 1–2% for major elements (>10 wt%) and 3–10% relative for minor elements (0.5–10%) As the detection limit is approached (<0.1 wt%), relative errors approach 100%. In some instances throughout the tex, we refer to informal thin section numbers of our probed samples. Supplemental[1] Table S1 provides corresponding formal IODP sample numbers.

Olivine crystals, Cr-spinel inclusions, and Cr-spinel phenocrysts were analyzed for major elements using a JEOL JXA-8230 Superprobe at the University of Iowa. For olivine, the beam conditions were set to 20 keV and 200 nA. Each spot was analyzed for 10.5 min with a dwell times of 40 s for major elements, 90 s for most minor elements, and 360 s for Al. To check for instrumental drift as well as ensure data quality, we analyzed San Carlos Olivine grains intermittently during the analysis. Cr-spinel was measured with the beam set to 20 keV and 20 nA and 1.5 min count time. The Cr-spinel standard NMNH 117075 was analyzed during the analysis as a drift monitor and for data quality assurance.

Thermobarometry and mineral-melt equilibria

The Fe/Mg partition coefficient between olivine and basaltic liquid [$(Fe/Mg)_{ol}/(Fe/Mg)_{melt}$] is well constrained experimentally as 0.30 ± 0.03 (Roeder and Emslie 1970) being constant for a wide range of conditions, except for pressures higher than 10 kbar (Ulmer 1989) or for Fe-rich olivine (Fo < 25) (Topliss and Carroll 1995). The Fe/Mg partition coefficient between orthopyroxene and basaltic liquid is also well established at 0.29 ± 0.06 (see Putrika 2008). The Fe/Mg partition coefficient between clinopyroxene and basaltic liquid is less well constrained than for olivine-liquid, principally because of the presence of abundant ferric iron in clinopyroxene. Although a slight compositional effect may exist (Hoover and Irvine 1977), $(Fe/Mg)^{cpx}/(Fe/Mg)^{melt} = 0.27 \pm 0.03$ is consistent with experimental results (Putirka 2008), and 0.27 is adopted here.

Estimates of temperatures and pressure of FAB crystallization are based on compositions of clinopyroxene phenocrysts and microlites using the methods, models, and equations of Putirka et al. (1996, 2003) and Putirka (2008). Specifically, we use Equations P1 and T1 of Putirka et al. (1996); the model of Putirka et al. (2003); and Equations 30 (temperature), 33 (pressure), and 34 (temperature) of Putirka (2008). Conditions of boninite crystallization are based on orthopyroxene and olivine phenocryst compositions. Pressure estimates from orthopyroxene are calculated from Equations 29a, 29b, and 29c of Putirka (2008) and temperatures are calculated from Beattie (1993) and Equations 28 and 28b of Putirka (2008). Olivine temperature estimates are calculated using Beattie (1993) and Equations 13–15 of Putirka (2008).

To compare the composition of clinopyroxene phenocrysts and microlites from Expedition 352 FAB with those from typical MORB, we collated clinopyroxene and complementary whole rock compositions from the Petrological Database (PetDB, http://www.earthchem.org/petdb). Details of sample selection, collation, and manipulation of PetDB MORB whole-rock and clinopyroxene samples are provided in the Supplemental Material[1]. Pressure and temperature estimates of clinopyroxene from the PetDB MORB database (n = 75 samples shown to exhibit clinopyroxene-melt equilibrium) are calculated using the thermometer of Putirka (2008, Eq. 33) and the barometer of Neave and Putirka (2017).

It is important to establish whether Expedition 352 FAB clinopyroxene phenocrysts and microlites and boninite orthopyroxene and olivine phenocrysts were in equilibrium with the host magma when they crystallized. If mineral-melt equilibria can be established, specific mineral-melt (whole-rock composition) pairs can then be used to constrain the pressure and temperature of crystallization. The demonstration of disequilibrium between specific mineral-melt pairs also yields information, such as the presence of xenocrysts and/or crystal cumulates.

To assess mineral-melt Fe-Mg exchange for clinopyroxene, orthopyroxene, and olivine for our new mineral compositions, we use whole-rock compositions from Reagan et al. (2015). Whole-rock Mg# [i.e., $Mg^{2+}/(Mg^{2+}+Fe^{2+})$ for the FAB] is calculated assuming $Fe^{3+}/FeT = 0.17$ (whereby $FeT = Fe^{2+} + Fe^{3+}$), a value that approximates crystallization at the fayalite-magnetite-quartz (FMQ) oxygen buffer. For the boninites, high-Mg andesites and lone anomalous andesite TS 93 (formal IODP number 352-U1439C-8R-2-W 105/107-TSB-TS_93), whole-rock Mg# is calculated assuming $Fe^{3+}/FeT = 0.22$, which corresponds to f_{O_2} of about +1 to 1.5 log units above FMQ (see Brounce et al. 2015).

Sample compositions and classification

We first establish lithology on the basis of whole-rock chemistry using a subset of Expedition 352 whole-rock analyses (Reagan et al. 2015) for which we have corresponding thin sections. The whole-rock analyses are used to classify magma types and calculations of the mineral-melt equilibria. Shipboard analyses were carried out using ICP-AES methods provided in Reagan et al. (2015). The effect of seawater alteration on whole-rock compositions is typically limited to the addition of K and in some cases Ca and Na to the whole-rock (Shervais et al. 2019), which has minimal effect on the thermobarometry calculations.

On the basis of whole-rock geochemistry, Expedition 352 lavas are divided into basalt-andesite-dacite-rhyolite and boninite series lavas on the basis of SiO_2 vs. MgO and MgO vs. TiO_2 (Figs. 2a and 2b). Boninites are further divided into basaltic boninite, low-Si boninite, and high-Si boninite on this plot based on approximate liquid lines of descent for primitive boninite with varying SiO_2 concentrations (Pearce and Reagan 2019). Highly differentiated boninite plots as high-Mg andesite (Fig. 2). The lavas from sites U1440 and U1441 all plot as basalts within the basalt-andesite-dacite-rhyolite field, whereas lavas from sites U1439 and U1442 plot as various types of boninite and high-Mg andesite.

Sample 352-U1439C-8R-2-W 105/107-TSB-TS_93 from boninite Site U1439, which is referred to as a high-Mg andesite below, is anomalous in that it plots within the basalt-andesite-dacite-rhyolite field series on the SiO_2 vs. MgO plot, but has low TiO_2 concentrations, which are more akin to those of high-Mg andesite.

Results

Petrography

The mineralogy and modal proportions of FAB, high-Mg andesite, and boninite are summarized in Table 1 and their principal petrographic characteristics are presented in Table 2. Representative thin-section photographs are provided in Figure 3.

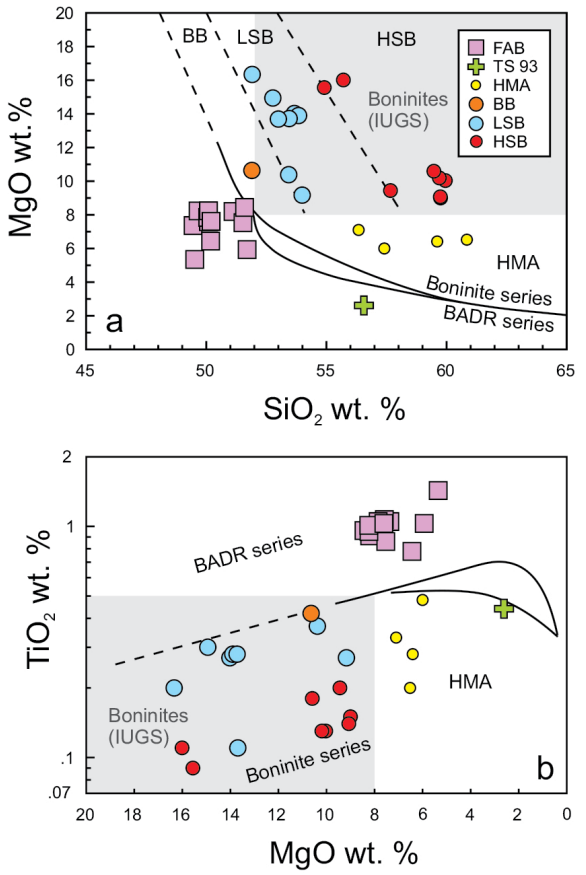

Figure 2. Whole-rock classification of Expedition 352 lavas. (**a**) MgO vs. SiO_2 of Expedition 352 magmas. The IUGS classification of boninites (gray shade) in **a** and **b** is from LeBas (2000). The boundaries between basalt-andesite-dacite-rhyolite (BADR) series and boninite series is from Pearce and Robinson (2010) and the subdivision of boninites into basaltic boninites (BB), low-Si boninites (LSB), and high-Si boninites (HSB) is from Reagan et al. (2015). The formal IODP number for TS 93 is 352-U1439C-8R-2-W 105/107-TSB-TS_93. (Color online.)

The FAB are generally aphyric with quench plagioclase, augite, and magnetite. Rare plagioclase and augite phenocrysts are present in some samples, the latter of which are almost always unzoned. Boninites are generally porphyritic. Low-Si boninites typically have phenocrysts of olivine, Cr-spinel, and clinopyroxene, sometimes with orthopyroxene. Groundmass often has quench clinopyroxene and plagioclase crystals. The high-Si boninites typically contain orthopyroxene ± olivine with Cr-spinel with quench orthopyroxene and clinopyroxene. Olivine crystals typically are subhedral to anhedral, whereas pyroxenes, plagioclase, and Cr-spinel are typically euhedral. In most boninites, olivine, clinopyroxene, and orthopyroxene phenocrysts are strongly zoned. The high-Mg andesites typically have augite ± orthopyroxene ± plagioclase and rare olivine phenocrysts with quench clinopyroxene and plagioclase in the matrix. Detailed petrographic descriptions are provided in the Supplemental Material[1].

Mineral compositions

The compositional data of all minerals are provided in the Supplemental Document (Supplemental[1] Tables S2–S7).

Olivine. EPMA analyses of olivine in the boninite are provided in Supplemental[1] Table S4. Olivine phenocrysts are highly magnesian ranging from Fo_{88} to Fo_{92} in the low-Si boninite and from Fo_{87} to Fo_{93} in the high-Si boninite. Apart from one rim of olivine in a low-Si boninite that has 0.15 wt% NiO, the remaining olivine NiO contents are high (0.22–0.43 wt%), approaching those of mantle olivine (cf. Sato 1977; Takahashi et al. 1987). CaO concentrations are low (0.13 to 0.20 wt%) and similar to those of olivine from water-rich subduction-related basalts (Gavrilenko et al. 2016).

Clinopyroxene. 118 analyses were acquired on clinopyroxene spanning all lithologies from all holes. Clinopyroxene analyses are provided in Supplemental[1] Table S2 and Figure 4a summarizes their compositional variation. All clinopyroxene in FAB, andesite, and high-Mg andesite are augite, with FAB clinopyroxene extending to more Fe-rich compositions ($Wo_{25}En_{44}Fs_{31}$ to $Wo_{42}En_{41}Fs_{18}$) compared with those from high-Mg andesite

Table 1. Modal estimates of phenocrysts and groundmass constituents of the FAB, lone andesite, high-Mg andesites, and boninites

Phase	FAB (*n* = 17)		TS 93 AND (*n* = 1)	HMA (*n* = 5)		BB (*n* = 8)		LSB (*n* = 14)		HSB (*n* = 13)	
	Mean %	Range %		Mean %	Range %	Mean %	Range %	Mean %	Range %	Mean %	Range %
Phenocrysts											
Olivine			–	0.6	0–3	6	1–14	8.9	0–30	2	0–10
Orthopyroxene			–	0.3	0–1	4	2–8	0.4	0–2	4.5	0–15
Clinopyroxene	1.2	0.3–2.0	2	2.3	0–15	3	1–5	1.1	0–6	0.1	0–0.5
Plagioclase	1.5	0.2–5	1	1.3	0–5						
Magnetite			–								
Chromite			–			0.7	0.5–1	0.8	0–1	0.01	0–0.1
Groundmass											
Orthopyroxene	–	–	–	1.6	0–10	15	10 –20	1	0–10	21	0–55
Clinopyroxene	20	8.0–35	–	15	8.0–25	22.5	10– 35	20	0–65	18	0–60
Plagioclase	38	10.0–53	37	38	25–55	50	50	14	0–50	–	–
Magnetite	2	1.0–3.0	–	1	0–3			–	–	–	–
Chromite	–	–	–	–	–			0	0–1	–	–
Glass (original %)	5.6	0–82	–	b	–	40	30–50	22	0–100	46	0–100
Mesostasis[a]	15	0–48	54	42	19–59	45	16–79	32	0–70	33	0–65
Vesicles	1.6	0–15	3	7	0–20	11	3–20	11	1.0–40	6	0–15

Notes: Abbreviations: FAB = forearc basalt; AND = andesite; HMA = high-Mg-andesite; BB = basaltic boninite; LSB = low-Si boninite; HSB = high-Si boninite. Phenocrysts include microphenocrysts; chromite typically occurs as inclusions in olivine.

[a] Mesostasis here refers to microlites and cryptocrystalline quench phases. Includes devitrified glass.

[b] One HMA has 73% glass; all of the others have 0%. Note that TS 93 is an anomalous andesite (see text).

TABLE 2. Summary of petrographic features of forearc basalts, boninites, and high magnesium andesites

Rock type	Phenocrysts	Microlites	Groundmass	Alteration	Textural features
FAB	PL: 0.1–1.5 mm CPX: 0.2–1.2 mm	PL CPX (rare)	Altered (oxidized) to unidentifiable secondary products; glass commonly devitrified	Oxidation of crypto-crystalline groundmass, veinlets of carbonates	Predominantly equigranular, intersertal and intergranular; minor subophitic relations
TS 93 AND	PL: 0.4 mm CPX: 0.6 mm	PL CPX	PL altered to zeolites in part, CPX altered to chlorite in part. Mesostasis completely altered to unidentified secondary products	zeolites, chlorite	Intersertal groundmass with augite phenocrysts
HMA	PL: 0.3–0.4 mm PX: <0.5 mm		Equigranular plagioclase set in cryptocrystalline groundmass	Groundmass plagioclase laths and cryptocrystalline materials ubiquitously altered/oxidized	Equigranular and intergranular, the latter of which is defined by the occupation of pyroxenes in the interstices of randomly oriented plagioclase laths
BB	OL: 0.4–7 mm OPX: 0.8–5 CPX: 0.2–5 CHR: 0.2–1	PL: 0.3 OPX: 0.2 CPX: 0.2	Glass or fine-grained mesostasis Typically altered to clay, zeolites and carbonate	Olivine phenocrysts occasionally replaced by clay, discrete zeolites	Phyric, hyalopilitic, OPX ML rimmed by CPX, OL mantled by OPX, rare glomerocrysts of OPX, rare oscillatory zonation of OPX, vesicles rare
LSB	OL: 0.3–3.0 mm OPX: 0.2–0.8 mm CPX: 0.3–0.5 mm CHR: 0.2 mm	OPX CPX	Predominantly hyalopilitic with clear fresh glass moderately altered glass rare	Minor carbonates and zeolites in veinlets	Phyric, hyalopilitic, OPX ML rimmed by CPX, OL mantled by OPX, rare glomerocrysts of OPX, rare oscillatory zonation of OPX, vesicles rare
HSB	OL: 0.1–1.6 mm OPX: 0.15–1.5 mm CPX: ≤0.2 mm	OPX CPX	Predominantly hyalopilitic with clear fresh glass; moderately altered glass rare	Oxidation and palagonitization of glass, veinlets of carbonates and glass	Phyric, OPX ML rimmed by CPX, glomerocrysts of OPX common, vesicularity up to 15%, devitrification spherules common

Notes: Abbreviations: FAB = forearc basalt; AND, andesite; HMA = high-Mg-andesite; BB = basaltic boninite; LSB = low-Si boninite; HSB = high-Si boninite. Note that TS 93 is an anomalous andesite (see text).

($Wo_{34}En_{51}Fs_{15}$ to $Wo_{42}En_{46}Fs_{12}$). Clinopyroxene from low-Si boninite vary primarily in terms of Mg and Ca, ranging from $Wo_{16}En_{71}Fs_{13}$ to $Wo_{43}En_{47}Fs_{10}$. Clinopyroxene from high-Si boninite is also augite ($Wo_{27}En_{56}Fs_{17}$ to $Wo_{48}En_{30}Fs_{22}$).

Clinopyroxene Al_2O_3 concentrations range from 2.10–7.68, 0.99–11.89, and 1.58–4.62 wt% in the low-Si boninite, high-Si boninite, and high-Mg andesite, respectively. Cr_2O_3 in the same order, ranges from 0.02–0.78, 0.01–0.38, and 0.01–0.56 wt%. FAB clinopyroxene have Al_2O_3 and Cr_2O_3, which range from 1.39–7.69 and 0–0.75 wt%, respectively. In general, TiO_2 contents of the Ca-rich pyroxene are variable and Na_2O contents are generally low (typically <0.25 wt%).

Mg#, Na_2O, TiO_2, and Cr_2O_3 contents of clinopyroxene show little systematic variation in FAB with depth (Fig. 5). In general, no appreciable differences exist between the composition of clinopyroxene cores and rims at similar core depths for the FAB, although Na_2O concentrations are somewhat higher in microlites relative to phenocrysts at similar depths in Core U1440B. Similarly, compositions of clinopyroxenes in boninite and high-Mg andesite show little variation with depth. Exceptions include general increases in Mg# and decreases in Na_2O content with depth for both boninite sites.

Low-Ca pyroxene. Analyses of low-Ca pyroxene are provided in Supplemental[1] Table S3. Low-Ca pyroxenes are found in the low-Si boninite, high-Si boninite, and high-Mg andesite but not in FAB (Fig. 4a). Low-Ca pyroxene in the low-Si boninite range from $Wo_1En_{89}Fs_{10}$ to $Wo_9En_{78}Fs_{13}$ and in the high-Si boninite, they range from $Wo_1En_{71}Fs_{10}$ to $Wo_5En_{89}Fs_{27}$. Orthopyroxene in the high-Mg andesite have a restricted range from $Wo_3En_{83}Fs_{14}$ to $Wo_5En_{77}Fs_{17}$. All low-Ca pyroxene are Mg-rich with X_{Mg} [100En/(En+Fs)] typically >85 (the mean X_{Mg} of all low-Si boninite and high-Si boninite low-Ca pyroxene is 86), although some high-Si boninite low-Ca pyroxene have X_{Mg} <80. X_{Mg} of low-Si boninite, high-Si boninite, and high-Mg andesite low-Ca pyroxene range from 83–90, 72–90, and 82–86, respectively. Rims are more iron-rich than their cores, with X_{Mg} typically 1–2 units lower than the cores. Orthopyroxene in the low-Si boninite, high-Si boninite, and high-Mg andesite have low Al_2O_3 (0.72–1.45, 0.26–1.61, and 0.92–1.90 wt%, respectively) and TiO_2 (typically ≤0.06%) (Supplemental[1] Table S3). Cr_2O_3 contents range from 0.07–0.70 wt% in the low-Si boninite, 0.05–0.90 wt% in the high-Si boninite, and 0.22–0.46 wt% in the high-Mg andesite.

Spinel. EPMA analyses of Cr-spinel are provided in Supplemental[1] Table S5. Cr-spinel occurs in both the low-Si boninite and high-Si boninite as reddish-brown, euhedral to subhedral crystals usually as inclusions in olivine but are also present in the groundmass. Cr-spinel in both the low-Si boninite and high-Si boninite have high Cr_2O_3 (52.8–62.8 and 55.8–62.9 wt%, respectively), which fall within the range of olivine-hosted spinel of Chichijima boninite (49–63 wt% Cr_2O_3, Dobson et al. 2006). Cr# are also high, ranging from 74–88 in low-Si boninite Cr-spinel and from 79–86 in high-Si boninite Cr-spinel (Supplemental[1] Table S5). In general, the very high Cr# of Cr-spinel reflect high Cr contents of host melts and low activities of Al. Mg# of the Cr-spinel in the low-Si boninite and high-Si boninite range from 54–65 and 50–62, respectively. Spinel Fe^{3+}/Fe^{2+} ranges from 0.22–0.42 in the low-Si boninite and from 0.15–0.34 in the high-Si boninite. Fe^{3+} is derived by stoichiometry using the methods of Droop (1987).

Magnetite is the only Fe-Ti oxide present and occurs only in the FAB. A single magnetite grain was analyzed and has MgO of 0.69 wt%, MnO of 0.37 wt%, and Al_2O_3 of 2.75 wt%, and TiO_2 of 17.11 wt% (Supplemental[1] Table S5).

Feldspar. Plagioclase is ubiquitous in FAB, the anomalous andesite 352-U1439C-8R-2-W 105/107-TSB-TS_93 and the high-Mg andesite but relatively rare in the low-Si boninite and absent from all but the most differentiated high-Si boninite. A total of 78 spot analyses were obtained on plagioclase from

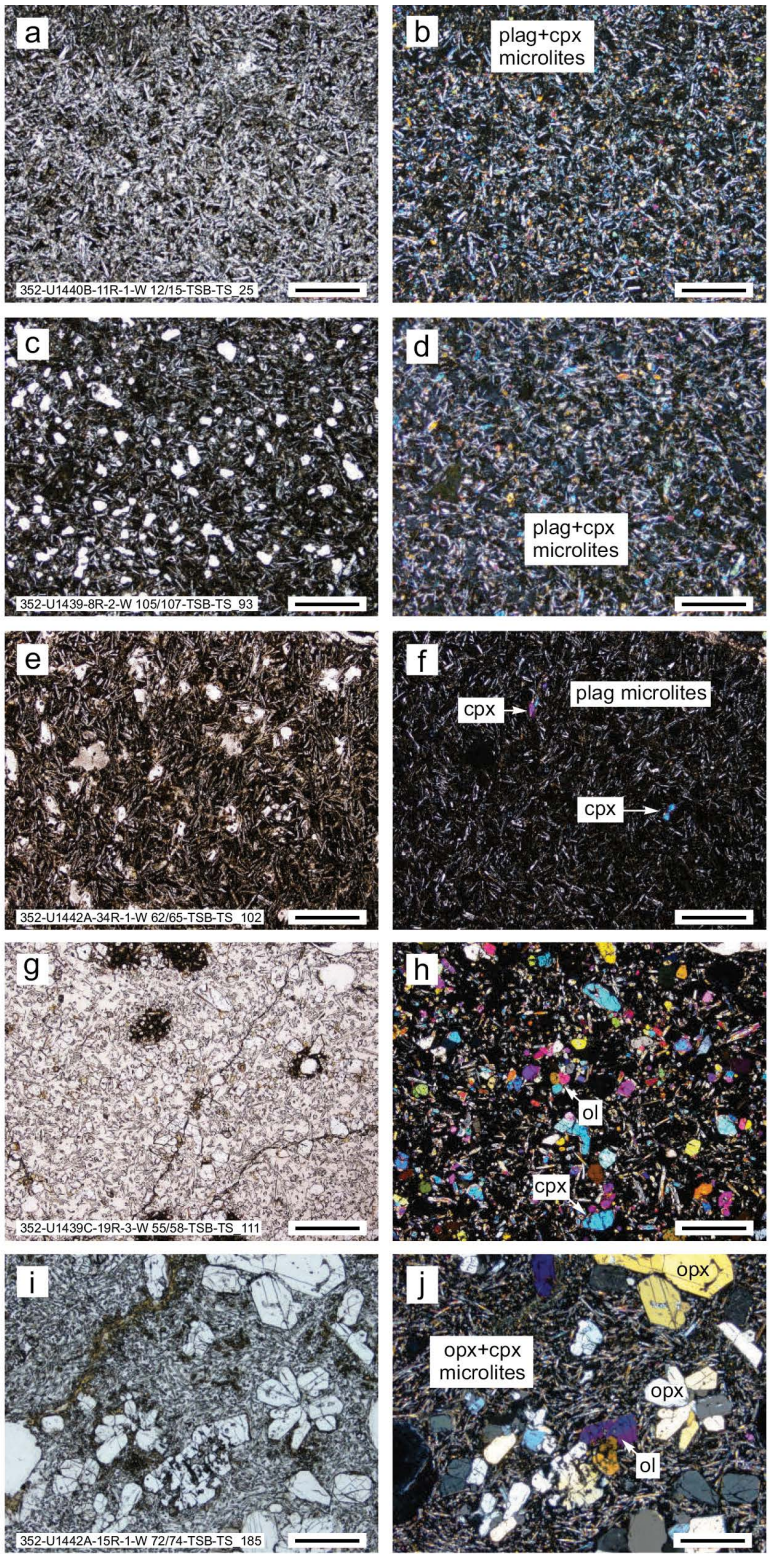

Figure 3. Photomicrographs of representative Expedition 352 lavas. (**a** and **b**) FAB (TS 50), (**c** and **d**) anomalous andesite (TS 93), (**e** and **f**) high-Mg andesite (TS 208), (**g** and **h**) low-Si boninite (TS 111), and (**i** and **j**) high-Si boninite (TS 185) under (**a**, **c**, **e**, **g**, **i**) plane-polarized light and (**b**, **d**, **f**, **h**, **j**) cross-polarized light. Scale bar in the lower right of each image is 1000 μm (1 mm). Formal IODP numbers for TS 50, TS 93, TS 208, TS 111, and TS 185 are shown on the bottom left-hand side of the plane-polarized images and all formal IODP numbers are provided in Supplemental[1] Table S1. (Color online.)

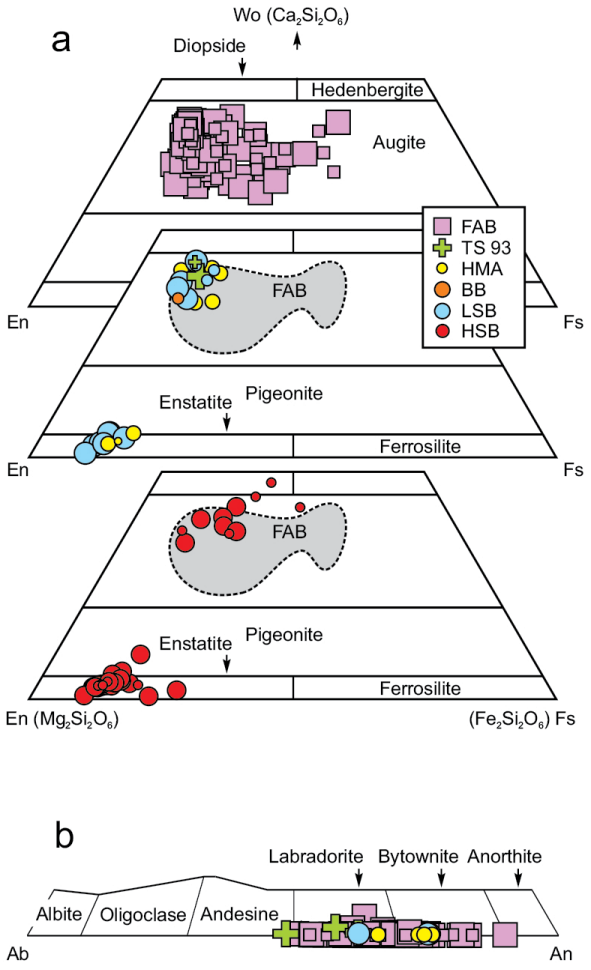

Figure 4. Mineral classification of Expedition 352 lavas. (**a**) FAB, anomalous andesite (TS 93), high-Mg andesite, and boninite clinopyroxene and orthopyroxene classification based on the En-Fo-Ws pyroxene quadrilateral (Morimoto 1988). The large spread in compositions of clinopyroxene is related to quench effects on rims and small grains. The large and small symbols represent cores and rims, respectively. (**b**) FAB, andesite, high-Mg andesite, and low-Si boninite plagioclase classification. (Color online.)

the FAB; 16 spot analyses were obtained on plagioclase of the anomalous andesite, high-Mg andesite, and low-Si boninite. The compositional range of plagioclase from the FAB nearly encompasses the compositions of plagioclase from all other magma types but extends to higher An content (FAB plagioclase cores record $An_{51–91}$ with a mean of An_{68}) (Fig. 4b, Supplemental[1] Table S6). For comparison, the range and mean of An from plagioclase of the andesite, high-Mg andesite, and low-Si boninite are $An_{49–62}$ (An_{56}), $An_{66–76}$ (An_{73}), and $An_{62–76}$ (An_{71}), respectively. Plagioclase cores were analyzed in FAB, the anomalous andesite, high-Mg andesite, and low-Si boninite; plagioclase rims were analyzed in the FAB only. In the FAB, plagioclase cores are normally zoned.

In the high-Mg andesite, plagioclase K_2O and FeO range from 0.03–0.04 and 0.75–0.98 wt%, respectively, whereas in plagioclase from the low-Si boninite, K_2O and FeO range from 0.07–0.13 and 0.87–1.04 wt%. FeO also ranges to much higher contents in the FAB (0.35–2.38 wt%) but FeO contents in the andesite plagioclase (0.75–0.80 wt%) are lower than all other magma types.

Conditions of crystallization

Pyroxene composition data were filtered such that only those with totals between 98.5–101 wt% oxides and with cations within 1% of 4 cations per 6 O (i.e., ±0.04) formula unit were used in thermobarometry calculations and related plots. Pressure and temperature estimates are shown for those clinopyroxene phenocrysts and microlites, and orthopyroxene and olivine phenocrysts, that pass the test of mineral-liquid equilibrium (Rhodes diagrams regions between dashed lines in Fig. 6). Table 3 and Figure 7 provide a synopsis of the pressure and temperature estimates obtained for all magma types using clinopyroxene and orthopyroxene thermobarometry and olivine thermometry. Figure 8 shows cores of MORB clinopyroxene in equilibrium and Figure 9 compares our calculated *P-T* estimates of these MORB with calculated *P-T* estimates of Expedition 352 FAB from this study. Whole-rock compositions are used as the input for the liquid in the thermobarometry calculations. Supplemental[1] Tables S7 and S8 provide results of pressure-temperature estimates on the basis of clinopyroxene thermobarometry and orthopyroxene thermobarometry, respectively; Supplemental[1] Table S9 provides temperature estimates on the basis of olivine thermometry. Supplemental[1] Tables S7–S9 provide an explanation of the calculation of the means and ranges cited in Table 3. Uncertainties in pressure and temperature estimates for all thermometers and barometers employed are ±1 kbar and ±30 °C, respectively.

Olivine-liquid thermometry. Most boninites from Expedition 352 have Mg# values of 80 to 83, which are too high to be in equilibrium with analyzed olivine crystals or for magmas in equilibrium with even highly depleted, Fo_{92}-bearing mantle (assuming $Kd_{Mg/Fe}$ between olivine and melt = 0.3 and melt $Fe^{3+}/FeT = 0.22$) (Fig. 6c, Supplemental[1] Table S9). To adjust our boninite whole-rock compositions toward equilibrium, as much as 22% accumulated olivine was subtracted from both low-Si and high-Si boninites. These adjusted whole-rock compositions have Mg# values in the range of 0.71–0.78, which are in keeping with magmas produced from depleted mantle (e.g., Roeder and Emslie 1970). Using these adjusted melt compositions and the olivine-liquid thermometry equation recommended for use when magmas are hydrous (Eq. 22 in Putirka 2008), and assuming 2 wt% H_2O in the melt that are average values measured in boninite pillow rind glasses from Chichijima (Dobson and O'Neil 1987), the low- and high-Si boninites yield similar ranges of calculated temperatures (1119–1202 °C).

A geohygrometer based on the distribution coefficient of CaO between magmas and olivine ($D_{CaO}^{Ol/L}$), and that is accurate to approximately 1.5 wt% was recently developed by Gavrilenko et al. (2016). The calculated water concentrations for Expedition 352 boninites using this geohygrometer are 2–4 wt% (Fig. 10). Using this range of water concentrations in Equation 22 from Putirka (2008), results in little change to the calculated olivine-liquid temperatures (i.e., using 4 wt% water results in calculated temperatures of 1120–1200 °C).

Clinopyroxene-liquid thermobarometry. Whole-rock Mg# vs. clinopyroxene Mg# relations are shown in Figure 6a for FAB,

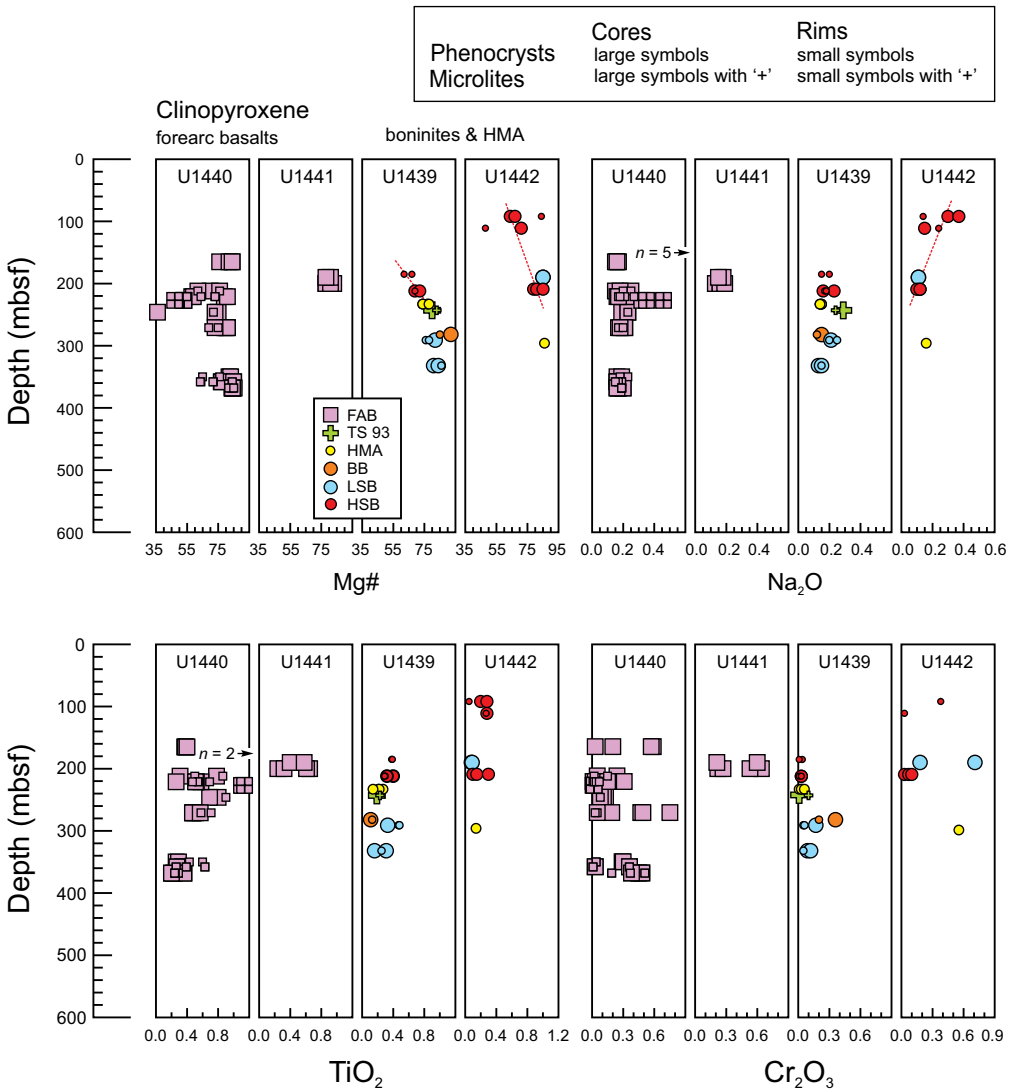

Figure 5. Expedition 352 clinopyroxene composition vs. sub-seafloor depth. Forearc basalt, andesite, high magnesium andesite, and boninite clinopyroxene Mg# (cationic $Mg/Mg+Fe^{2+}$), Na_2O, TiO_2, and Cr_2O_3 vs. depth in meters below sea floor (mbsf). Note that in the Na_2O vs. depth plot, five forearc basalt clinopyroxenes (154 m depth) plot off the right of the plot with anomalously high Na_2O ranging from 1.93–2.49 wt% and that in the TiO_2 vs. depth plot, two forearc basalt clinopyroxenes plot off the right of the plot with anomalously high TiO_2 of 1.22 and 1.89 wt%. (Color online.)

the andesite, high-Mg andesite, and boninites. Eleven analyses of clinopyroxene from the FAB, but none from the andesite and basaltic boninite, plot within the equilibrium field (Fig. 6a); a large number of clinopyroxenes from the FAB, high-Mg andesite, and boninite plot below the equilibrium field suggesting that they crystallized from differentiated interstitial magma.

The calculated temperatures of clinopyroxene phenocrysts and microlites from the FAB [when $K_D(Fe\text{-}Mg)^{Cpx\text{–}Liq} = 0.27 \pm 0.3$] are narrow, yielding a mean temperature of 1163 ± 14 °C in the range of 1142–1190 °C (n = 13), although the estimated pressure range is relatively large (0.5–4.6 kbars) (Table 3, Supplemental[1] Table S7). Phenocryst cores and rims, and microlites, show similar pressure and temperature estimates in accord with Scruggs and Putirka (2018).

As a test of equilibrium, we use Putirka (1999) to predict the clinopyroxene end-member components Di+Hd (DiHd), En+Fs (EnFs), CaTs, and Jd, using the liquid composition and estimated temperature and pressure as input. These predicted components represent the clinopyroxene composition that should precipitate if the liquid used as the input is saturated with clinopyroxene at the given temperature and pressure conditions. The components should also sum to one. If the sum is greater than one, then the system is oversaturated in clinopyroxene, and for a system where the sum is less than one, the liquid is undersaturated. These predicted components are also compared to the observed components for a given clinopyroxene as calculated by Putirka (1999, 2008). If the components match within model error, then the pressure–temperature–composition conditions are allowably within an equilibrium state and the pressure–temperature estimates are assumed to be valid. These clinopyroxenes also pass

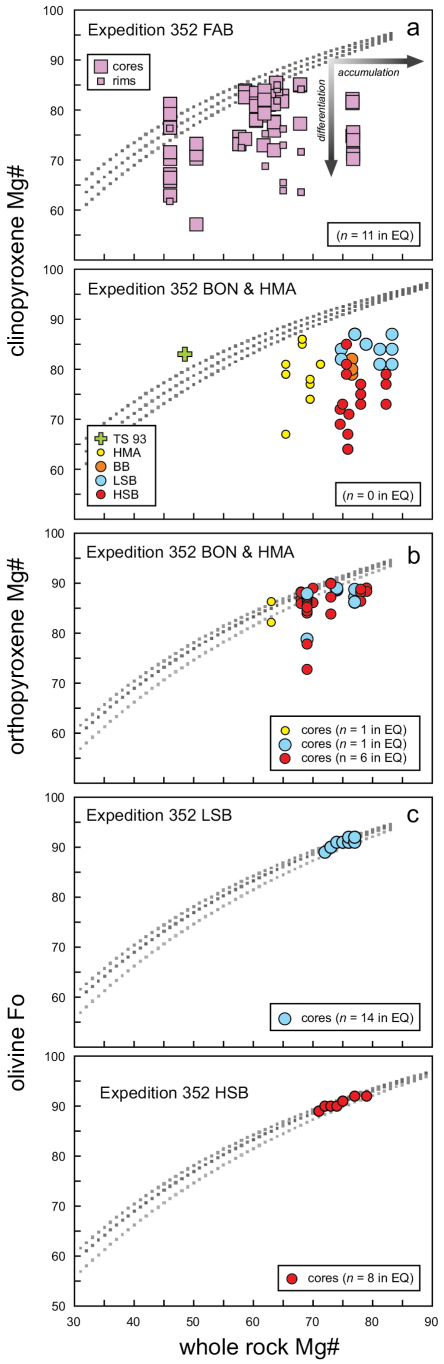

Figure 6. Mineral-melt Fe/Mg equilibrium diagrams for Expedition 352 lavas. (**a**) clinopyroxene, (**b**) orthopyroxene, and (**c**) olivine of FAB, andesite, high-Mg andesite and boninite varieties. In **a**–**c**, the Mg# is calculated assuming Fe^{3+}/Fe^{2+} = 0.17 of FeT and the equilibrium fields are represented by the dashed gray lines (Rhodes diagram). In **a**, the equilibrium field for Fe/Mg exchange between clinopyroxene and basaltic melt is 0.23 ± 0.05 (Topliss and Carroll 1995). In **b**, the equilibrium field for Fe/Mg exchange between orthopyroxene and basaltic melt is 0.29 ± 0.06 (Rhodes et al. 1979). In **c**, the equilibrium field for Fe/Mg exchange between olivine and basaltic melt is 0.30 ± 0.03 (Roeder and Emslie 1970). The Mg# of the whole rocks was corrected by olivine subtraction so that the samples lie along the equilibrium curve. (Color online.)

additional tests of equilibrium if the predicted and measured end-member components (DiHd, EnFs, and CaTs) match to within 2σ uncertainties (Supplemental[1] Fig. S1a).

We also calculated crystallization temperatures of clinopyroxene in equilibrium with MORB (Fig. 8) for comparison with FAB crystallization temperatures. The mean and range of PetDB MORB (n = 75) temperatures are 1182 ± 15 and 1133–1240 °C (Table 3, Supplemental[1] Table S10). The mean MORB temperature is close to that obtained on clinopyroxene from Expedition 352 FAB (1163 ± 14 °C) (Fig. 9a). Pressure estimates obtained from clinopyroxene in the Expedition 352 FAB (mean and range of 2.4 ± 0.4 and 0.5–4.6 kbar) are also similar to those calculated for the PetDB MORB data set (mean and range of 1.4 ± 0.2 kbar, –1.8–8.3 kbar, Fig. 9b, Table 3, Supplemental[1] Table S10). Nonetheless, crystallization temperatures of FAB relative to MORB at a given pressure are demonstrably lower (Fig. 9b). In contrast, melting temperatures and pressures are higher than MORB (Shervais et al. 2019). A plot of observed vs. predicted clinopyroxene components of the 75 PetDB MORB samples demonstrates that the data are as robust (Supplemental[1] Fig. S1b) as that of our clinopyroxene data from the Expedition 352 FAB (Supplemental[1] Fig. S1a).

Orthopyroxene-liquid thermobarometry. Whole-rock Mg# vs. orthopyroxene Mg# relations are shown in Figure 6b for the high-Mg andesite, low-Si boninite, and high-Si boninite. Several orthopyroxenes from the high-Mg andesite, low-Si boninite, and high-Si boninite fall within the orthopyroxene-basaltic melt equilibrium field.

Calculated orthopyroxene-melt equilibrium pressures and temperatures for Expedition 352 high-Mg andesite, low-Si boninite, and high-Si boninite (FAB have no orthopyroxene) are given in Table 3. Mean pressure and temperature estimates for the single high-Mg andesite provide 0.2 ± 0.05 kbar and 1193 ± 26 °C (Table 3), respectively. *P-T* conditions determined for the low-Si and high-Si boninites based on orthopyroxene thermobarometry are 0.3 ± 0.1 kbar (mean) and 1214 ± 13 °C (mean) and 0.2–0.4 kbar (mean of 0.3 ± 0.1 kbar) and 1235–1264 °C (mean of 1249 ± 13 °C), respectively (Table 3, Supplemental[1] Table S8). The temperatures calculated for orthopyroxene are higher than those calculated for olivine from the low-Si boninite and high-Si boninite, which agree with each other within the uncertainties of the calculations (see Table 3). As orthopyroxene normally follows olivine in the boninite liquid lines of descent (Pearce and Reagan 2019), the higher calculated orthopyroxene temperatures are surprising. Possible reasons for the higher boninite orthopyroxene crystallization temperatures are discussed in the Discussion (*P-T* evolution of FAB and boninite).

Inferences from spinel compositions. Plots of TiO_2 vs. Cr# and TiO_2 vs. Al_2O_3 of olivine-hosted chromite of the low-Si boninite and high-Si boninite, demonstrate their very low, arc-like TiO_2 and Al_2O_3 and high Cr# relative to MORB spinel (Figs. 11a and 11b). A plot of Cr# vs. Mg# in chromite demonstrates a compositional overlap of low-Si boninite and high-Si boninite chromite with Izu-Bonin (Leg 125; van der Laan et al. 1992) and Chichi-jima (Umino 1986; Yajima and Fujimaki 2001) boninite spinel, and a close similarity between Expedition 352 boninite spinel and boninite spinel from the Semail ophiolite (Fig. 11c) (Ishikawa et al. 2002).

Table 3. Thermobarometry summary

Rock type	Thermobarometer	*n*	*P*, μ (kbar)	*P*, range (kbar)	*T*, μ (°C)	*T*, range (°C)
FAB	Clinopyroxene	11	**2.4 ± 0.4**	0.5–4.6	**1163 ± 14**	1142–1190
HMA	Orthopyroxene	1	**0.2 ± 0.05**	–	**1193 ± 26**	–
LSB	Orthopyroxene	1	**0.3 ± 0.1**	–	**1214 ± 9**	–
HSB	Orthopyroxene	6	**0.3 ± 0.1**	0.2–0.4	**1249 ± 13**	1235–1264
LSB	Olivine	14	–	–	**1172 ± 23**	1119–1202
HSB	Olivine	8	–	–	**1152 ± 24**	1125–1190
PetDB MORB	Clinopyroxene	75	**1.4 ± 0.2**	(–1.8–8.3)	**1182 ± 15**	1133–1240

Notes: Refer to Supplemental[1] Tables S10–S12 for specific thermobarometers employed. Uncertainties associated with estimated *P* and *T* are ±1 kbar and ±30 °C, respectively. Means are in bold and uncertainty assigned to the mean is the standard deviation.

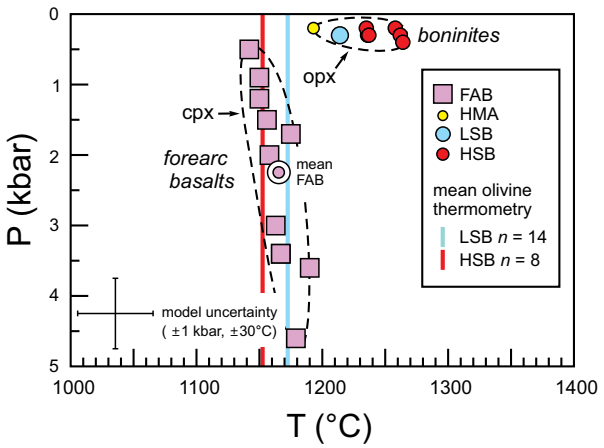

Figure 7. Pressure-temperature summary plot. Plot shows the mean estimated pressures and temperatures calculated via clinopyroxene and orthopyroxene thermobarometry and olivine thermometry. Uncertainties in the pressure and temperature estimates are ±1 kbar and ±30 °C, respectively. (Color online.)

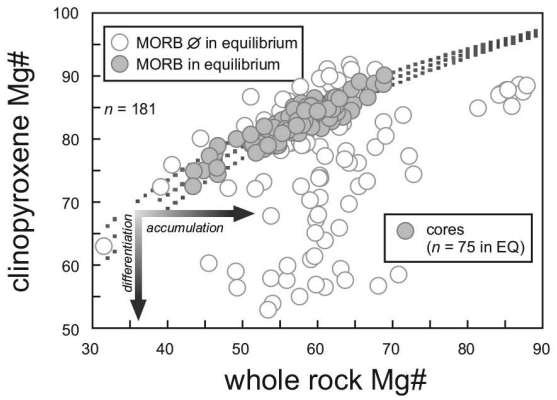

Figure 8. Mineral-melt Fe/Mg equilibrium diagram for PetDB MORB clinopyroxenes. The equilibrium field for Fe/Mg exchange between clinopyroxene and basaltic melt is 0.27 ± 0.03 (Topliss and Carroll 1995) and is represented by region enclosed by dashed lines (Rhodes diagram).

A plot of Cr# vs. TiO_2 wt% for chromite with vectors showing melt-rock reactions between refractory mantle compositions and melts generated by partial melting of these sources (Pearce et al. 2000) is shown in Figure 12. MORB composition melts have

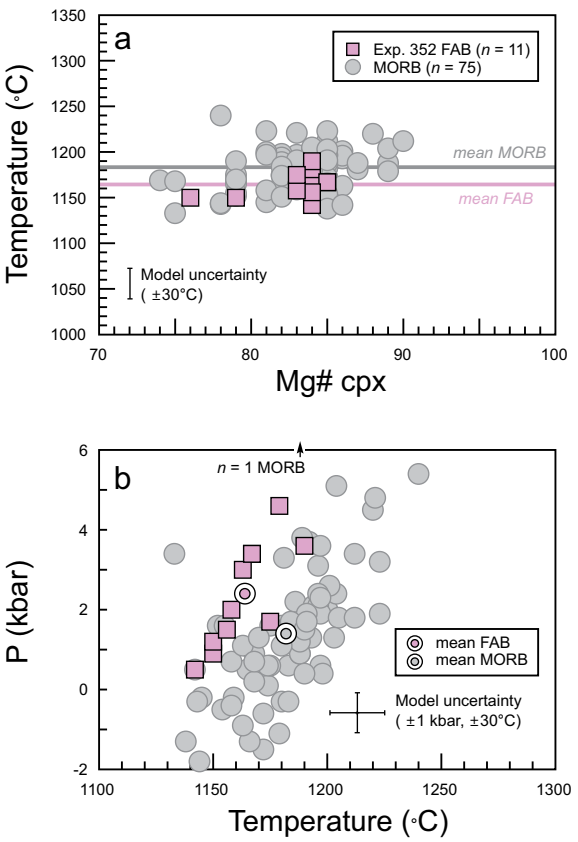

Figure 9. Temperature vs. Mg # and pressure of Expedition 352 FAB clinopyroxene vs. MORB clinopyroxene. In **a** and **b** means only are plotted; standard deviations are provided in Table 3. In **b**, the larger white circles enclosing a smaller purple and gray circle represent the mean temperature and pressure estimates of Expedition 352 FAB and MORB clinopyroxenes, respectively. Note also in **b** that one PetDB MORB sample (MELPROT-5-037-001) plots off the top of the figure with a *P* of 8.3 kbar and temperature of 1188 °C. See Table 3 and Supplemental Material[1] for details of calculation of FAB and MORB clinopyroxene temperature estimates. (Color online.)

relatively high Al/Cr ratios and high TiO_2, whereas boninite-related melts are more refractory, with low Cr/Al ratios and lower TiO_2. This plot demonstrates that chromite of the Expedition 352 low-Si and high-Si boninites overlap with the field of chromite in other IBM boninites (see Pearce et al. 2000 for references) in Cr# vs. TiO_2 wt% space. The Expedition 352 spinels also plot at the end of the melt-mantle interaction trends that characterize the

drilled harzburgites from Conical seamount in the IBM forearc. Thus, the compositions of Expedition 352 chromite support the genetic link between boninites and depleted mantle lithosphere in the forearc (Parkinson et al. 1998).

Dare et al. (2009) used spinel compositions to calculate f_{O_2} using the method of Ballhaus et al. (1991), and demonstrated that chromite from MORB, island arc basalts and subduction initiation boninites can be discriminated on plots of $\Delta\log f_{O_2}$ fayalite-magnetite-quartz (FMQ) vs. Cr#. Compared to MORB spinel, island arc spinel was shown to have higher f_{O_2} and similar-to-higher Cr#, reflecting the fact that fluid-rich oceanic subduction environments typically lead to more oxidizing conditions and higher degrees of melting than ocean ridges. Boninites were shown to have higher Cr# than both MORB and island arc basalts, and oxygen fugacities that span MORB and arc values reflecting prior mantle depletion and variable f_{O_2} in subduction components.

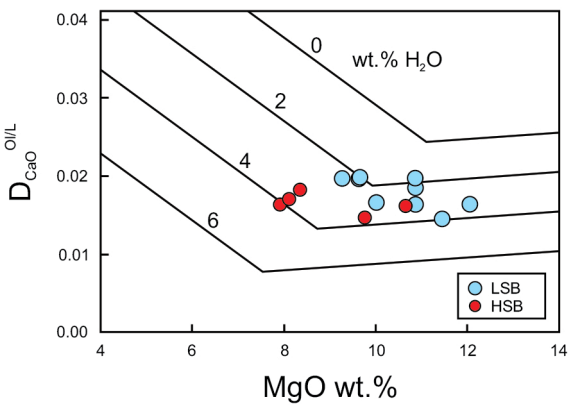

Figure 10. Geohygrometer based on the distribution coefficient of CaO between magmas and olivine ($D_{CaO}^{O/L}$) vs. MgO of Exp. 352 boninite, which is accurate to approximately 1.5 wt% (Gavrilenko et al. 2016). (Color online.)

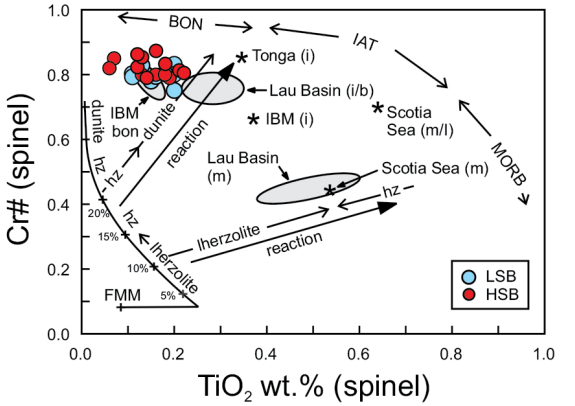

Figure 12. Spinel Cr# vs. TiO_2 relations of Expedition 352 boninites. The plot (Pearce et al. 2000) demonstrates that Expedition 352 boninites overlap with the field of Cr-spinel in other IBM boninites (see Pearce et al., for references) and supports the model in which some boninite melts also refertilize the forearc mantle lithosphere upon ascent to the surface (Parkinson et al. 1998). (Color online.)

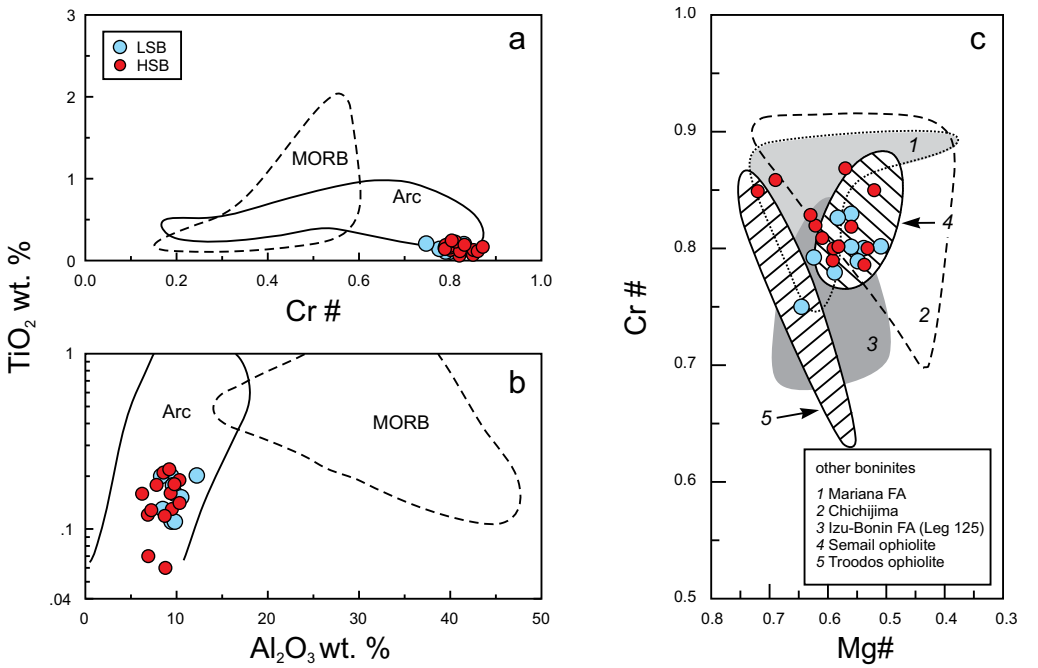

Figure 11. Tectonomagmatic discrimination of Expedition 352 boninites on the basis of chromian spinel composition. (**a**) Chromian number (Cr#, cationic Cr/Cr+Al) vs. TiO_2 (Arai 1992), (**b**) Al_2O_3 vs. TiO_2 (Kamenetsky et al. 2001), and (**c**) Mg vs. Cr# number of boninite spinel inclusions in olivine. Shown for comparison in **c** are the fields of boninite spinel compositions of (1) the Mariana forearc (Bloomer and Hawkins 1987), (2) Chichijima (Umino 1986; Yajima and Fujimaki 2001), (3) the Izu-Bonin forearc (Leg 125, van der Laan et al. 1992), (4) the Semail ophiolite (Ishikawa et al. 2002), and (5) the Troodos ophiolite (Cameron 1985). (Color online.)

Our oxygen fugacity data reported in Supplemental[1] Table S11 are plotted in Figure 13 together with the fields from Dare et al. (2009). Although the errors are high for calculated f_{O_2} ($Fe^{3+}/\Sigma Fe$ values were not quantified using Mössbauer spectrometry), the Expedition 352 boninites plot in the center of the boninite field with no overlap into other fields. Specifically, boninites exhibit $\Delta\log f_{O_2}$ FMQ of 0.1–1.1 with no significant differences between low- and high-Si varieties. Despite their lower precision, these f_{O_2} values are mostly within the range of ca. 0.3–1.5 obtained from Fe^{3+}/Fe^{2+} measurements on glasses from FAB and (younger) boninites from the IBM system (Brounce et al. 2015). The high Cr# and moderately high calculated f_{O_2} values for chromite from Expedition 352 boninites are similar to those of ophiolitic boninites (e.g., Dare et al. 2009).

Discussion

P-T evolution of FAB and boninite

A plot of Mg# of FAB and MORB clinopyroxene vs. temperature estimates (Fig. 9) shows that FAB clinopyroxenes crystallize at 1142–1190 °C within the range of MORB (1133–1240 °C), but at slightly higher pressure (~0.2–0.5 kbar) than MORB (Fig. 9b), which is at the edge of model uncertainty.

The olivine-liquid data in Figure 7 demonstrate that the crystallization temperatures for relatively primitive boninites (1119–1202 °C, with means and standard deviations of 1172 ± 23 and 1152 ± 24 °C for the low-Si boninites and high-Si boninites, respectively) overlap with clinopyroxene crystallization temperatures for somewhat more differentiated FAB (1142–1190 °C with a mean of 1163 ± 14 °C; Table 3). Clinopyroxene in FAB, however, records higher pressures (0.5–4.6 kbar with a mean of 2.4 ± 0.4 kbar) than for orthopyroxene crystallization in boninites (0.2–0.4 kbar with a mean of 0.3 ± 0.1 kbar) (Table 3). These calculations infer that FAB crystallization began at marginally higher temperatures and occurred over a broader range of pressures compared with boninites, which is consistent with higher *P-T* conditions calculated for FAB generation compared with boninite (Shervais et al. 2019; Lee et al. 2009).

We estimate densities of FAB and boninite (Fig. 14) to assess relative rates of magma ascent to better understand why FAB and boninite exhibit different crystallization pressures (lower pressures and temperatures for the latter). We estimate density for the cases of dry and hydrous compositions (FAB with 0.3 wt% dissolved H_2O and boninite with 3 wt% dissolved H_2O) using the models of Lange and Carmichael (1990) and Ochs and Lange (1999), respectively, which make use of the major oxide composition of a liquid.

Boninites have significantly higher concentrations of MgO (9.00–16.34 wt%) compared with FAB (5.40–8.35 wt%), causing the boninites to be less dense (calculated dry and wet densities of 2.65–2.69 and 2.46–2.50 g/cm^3 for the low-Si boninites and 2.59–2.68 and 2.41–2.49 g/cm^3 for the high-Si boninites) compared with FAB (dry density of 2.70–2.77 g/cm^3 and wet density of 2.68–2.74 g/cm^3). On the basis of differences in pressure, and hence depth, of formation of FAB magma at ~14–16 kbar or 47–53 km (Shervais et al. 2019) and pressure and depth of crystallization of the FAB (0.5–4.6 kbar or 2–15 km), the FAB magma traveled about 30–50 km before crystallizing clinopyroxene. In contrast, taking into consideration the pressure and depth of boninite magma formation (assuming 3 wt% water) at 4–12 kbar or 13–40 km (Shervais et al., in review) and the pressure and depth of boninite crystallization at 0.2–0.4 kbar or 0.7–1.3 km, the boninite magma traveled between about the same distance before crystallizing orthopyroxene. The presence of water lessens the density of silicate melts due to its low molecular weight (Lange 1994) and under similar magma network conditions (e.g., melt conduit/pipe diameter or dike width, and wall rock density), less dense melts will ascend faster than denser ones (e.g., Tanaka et al. 2014). The lesser density of the boninite relative to the FAB is consistent with the former being more buoyant. In addition to a significantly shorter travel time from place of magma generation to site of crystallization, the lower density allowed the boninite to rise faster and to shallower levels and erupt more rapidly, thus preserving the temperatures of their near-primary magmas (Table 3). It should be noted, however, that most Exp. 352 boninites analyzed here erupted with accumulated

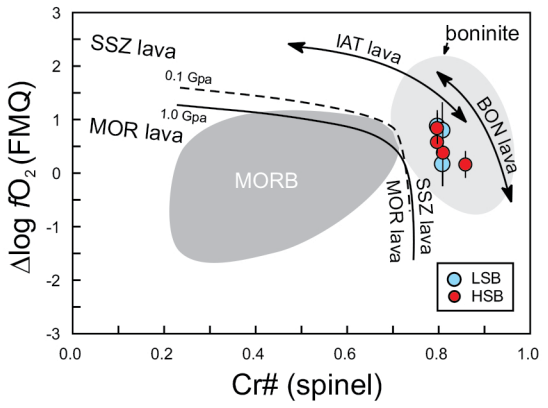

Figure 13. Plot of $\Delta\log f_{O_2}$ fayalite-magnetite-quartz (FMQ) vs. spinel Cr# (Dare et al. 2009) of Expedition 352 boninites. f_{O_2} is calculated by the method of Ballhaus et al. (1991). Supplemental[1] Table S12 gives values and errors. (Color online.)

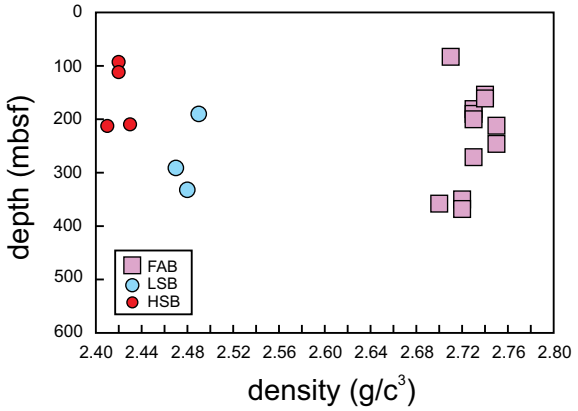

Figure 14. Depth vs. density of FAB and boninite assuming 0.3 and 3 wt% dissolved H_2O in the FAB and boninite magma, respectively. Error bars represent ±1 standard deviation but in all cases, the uncertainty of the error is smaller than the symbol size. Densities were calculated from Ochs and Lange (1999). (Color online.)

crystals adding to boninite density and making it less eruptible. However, olivine and pyroxenes tend to be approximately 20% more dense than their basalt parent, so if a rock contains 10–20% olivine phenocrysts, the fractional increase in density is only 0.02–0.04, which would not significantly affect density, and hence ascent and eruptibility, particularly as the boninite magmas were volatile saturated. Significant density differences between the FAB and boninite thus suggests that the latter rose faster from their source than FAB, thus preserving relatively high crystallization temperatures.

The average mantle separation temperature for FAB (the last temperature of magma-mantle equilibration) is 1380 °C at 15 kbar (Shervais et al. 2019) and our calculated clinopyroxene temperatures are 1179 °C at 4.6 kbar to 1142 °C at 0.5 kbar (Supplemental[1] Table S8). Thus, the cooling rate for the shallow part of the system (9.02 °C/kbar or about 2.72 °C/km) is about half that calculated for magma to get from its source at 15 to 4 kbar (19.3 °C/kbar or 5.9 °C/km), which may be the result of latent heat release during crystallization at crustal pressures. Low-Si boninite, however, typically last equilibrated with mantle at 0.8 kbar and 1270 °C with 3 wt% water (Shervais et al., in preparation). Our olivine crystallization temperatures record fractionation starting at 1202 °C (Supplemental[1] Table S10) and our orthopyroxene barometry suggests fractionation at 0.3 kbar (Table 3). This yields a rapid cooling rate of greater than 100 °C/kbar or >30 °C/km, significantly higher than for FAB. However, the calculated orthopyroxene crystallization temperatures of 1214 °C for the low-Si boninite and 1235–1264 °C for the high-Si boninite (Table 3, Supplemental[1] Table S8), suggest that crystallization histories for the boninites are complex.

The increase in crystallization temperature for boninite orthopyroxene relative to boninite olivine is surprising as the former follows the latter in the liquid line of descent for boninite (Pearce and Reagan 2019) and so is expected to yield a lower crystallization temperature. The significant temperature increase indicates a significant contribution of latent heat to the thermal budget that could be the result of, for example, a heating event by hotter, more mafic magma just prior to eruption (e.g., Venezsky and Rutherford 1999; Devine et al. 2003). Alternatively, Blundy et al. (2006) argued that temperature increase in Mount St. Helens (Washington, U.S.A.) and Shiveluch (Kamchatka, Russia) andesitic magmas were caused instead by latent heat release of crystallization via magma decompression and degassing, which they contend is likely in any hydrous magma that decompresses at a rate that permits crystallization and heat retention. This may be the case in the Exp. 352 boninite (Fig. 15).

Comparison of crystallization temperature and pressure with other IBM boninites

Expedition 352 boninites record crystallization temperatures similar to those of other Izu-Bonin boninites. Expedition 352 low-Si and high-Si boninite olivine temperature estimates (means of 1172 ± 23 and 1152 ± 24 °C, respectively) and orthopyroxene temperature estimates (means of 1214 ± 9 and 1249 ± 13 °C, respectively) fall within the temperature range obtained via pyroxene thermometers on boninites (1080–1287 °C, Dobson et al. 2006; Supplemental[1] Table S12) from Chichijima (~160 km SSW of Expedition 352 Sites). The range of <1100–1260 °C calculated via phase relations for Izu-Bonin forearc (Site 786, Ocean Drilling Program) boninites by van der Laan et al. (1992) also encompasses the range in temperatures estimated for Expedition 352 low-Si boninites on the basis of orthopyroxene thermometry, and high-Si boninites on the basis of orthopyroxene and olivine thermometry within the uncertainties (Table 3, Supplemental[1] Table S12). Thus, temperatures largely overlap for all boninites from the Bonin Islands region.

Comparisons of FAB to MORB and the Semail ophiolite

Here, we compare our results for the IBM forearc lavas with MORB and ophiolites to test the hypothesis that the birthplace of ophiolites is a proto-arc/forearc environment formed during subduction initiation. Such data also illustrate changes in condi-

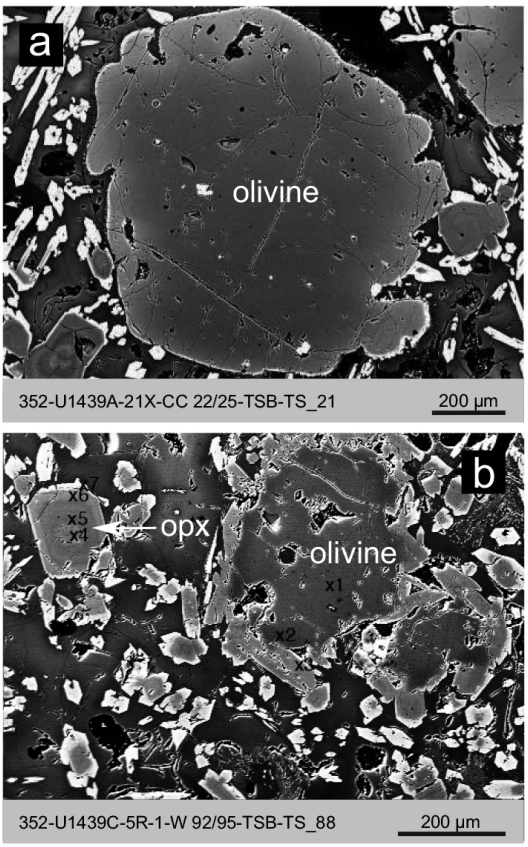

Figure 15. SEM-BSE images of resorbed olivine in Exp. 352 high-Si boninite. (**a**) Sample U1439A 21X-CC 22/25. Resorbed olivine (with chromite inclusions). This olivine has a very thin Fe-rich rim suggesting that olivine started to grow again from the melt about the time of cooling associated with eruption. This texture may be explained by olivine growth from primitive high-Si boninite, resorption by heating during rapid orthopyroxene growth, followed by saturation at the end during eruption as the system cooled (**b**) Sample 352-U1439C-5R-1-W 92/95-TSB-TS_88. Our interpretation is that olivine first grew from a melt that became more magnesian probably due to mixing with a more mafic magma. This was followed by resorption and orthopyroxene growth on the resorbed olivine. We interpret this olivine resorption to possibly be the result of heating due to early orthopyroxene growth (note the composition of the orthopyroxene immediately surrounding the olivine that is the same as the outer zone (spot 6) of the nearby orthopyroxene to the left).

tions of magma differentiation as the geodynamics of volcanism evolved after subduction initiation. First, we use discrimination diagrams for FAB (below) and then boninites (next section) to compare conditions of crystallization with lavas from known tectonic settings.

In the Oman ophiolite, initial MORB-like lavas (lower Geotimes Unit) were followed by the eruption of arc-like basalts (Lasail and Alley units; Alabaster et al. 1982). The time progression from less LILE-depleted and HFSE-enriched lavas to LILE-enriched and HFSE-depleted compositions defines the subduction initiation rule of Whattam and Stern (2011) and is characteristic of other ophiolites, e.g., Mirdita (Dilek et al. 2008) and Pindos (Saccani and Photiades 2004) and the Central American forearc (Whattam et al. 2020). In Figure 16a, we show that 93% of the clinopyroxene from Expedition 352 FAB plot to the right (high TiO_2 side) of a line of $Cr_2O_3 = (5.28 \times TiO_2) - 2.62$ drawn here to separate FAB from boninite (more depleted melt compositions lie left of the line). The Expedition 352 FAB clinopyroxene plot along with 97% of MORB (n = 1198), whereas 81% of the boninite clinopyroxenes plot to the left of this line. We take the decrease in Ti and increase of Cr concentrations in clinopyroxene from lower FAB to upper FAB and boninite to be a reflection of the concentrations of these elements in their associated melts, which suggests increasing depletion of the magma sources with time. All of the MORB-like Geotimes Unit basalts of Oman plot to the right of the line of $Cr_2O_3 = (5.28 \times TiO_2) - 2.62$ and the majority of the arc-like Alley Unit (79%) plot to the left of this line (Fig. 16b) indicating a similar increased depletion with stratigraphic height. The plot does not effectively discriminate the arc-like Lasail Unit of Oman, however, as 79% of lavas of this unit plot with the FAB and MORB and 65% of lavas of the arc-like Cpx-phyric unit plots to the left of the line with the Alley Unit lavas.

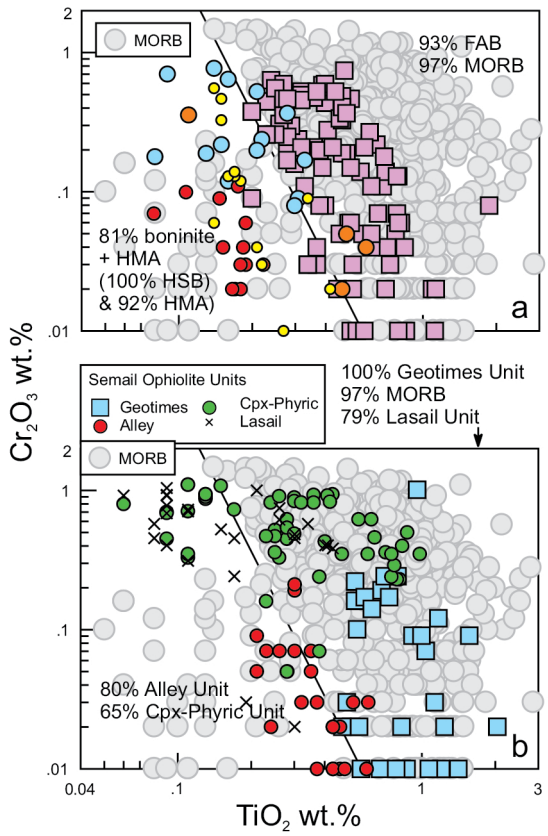

Figure 16. Subdivision of Expedition 352 FAB and boninites vs. Semail ophiolite lavas on the basis of clinopyroxene Cr_2O_3 vs. TiO_2 relations. (**a**) Expedition 352 FAB and (**b**) Semail ophiolite lavas (Alabaster et al. 1982).The sub-vertical line is $Cr_2O_3 = (5.28 \times TiO_2) - 2.62$. (Color online.)

Implications for ophiolite and forearc crust formation

Originally interpreted as "trapped" West Philippine Basin back arc basin crust generated prior to subduction inception (DeBari et al. 1999, see Fig. 1 for location of their study), FAB were instead interpreted by Reagan et al. (2010) as the first lavas formed after subduction initiation due to decompression melting of the mantle during forearc spreading (Kodaira et al. 2011). This model is similar to that first proposed by Stern and Bloomer (1992) and that was later refined to include ophiolite petrogenesis by Shervais (2001), Whattam and Stern (2011), and Stern et al. (2012).

On the basis of clinopyroxene thermobarometry and chemistry from this study, the FAB exhibit mostly MORB-like tectonomagmatic affinities with crystallization pressures and temperatures on the high-P, low-T side of the MORB array. These findings lend credence to the idea of an origin for FAB by seafloor spreading, albeit above a newly subducting slab (e.g., Reagan et al. 2010; Shervais et al. 2019), which may explain the steeper trajectory of cooling for FAB relative to MORB.

We suggest that, in the case of the present study area, initial partial melting of previously depleted mantle (Yogodzinski et al. 2018; Li et al. 2019) during seafloor spreading at source depths lower than those of MORB (46–53 vs. ~60–80 km), and at higher temperatures (Shervais et al. 2019) produced FAB (Fig. 17). The unusually high temperatures of melting to generate FAB might have originated in the Manus Plume, which has been interpreted to have surfaced in the Bonin island region about the time of subduction initiation (Macpherson and Hall 2001; Wu et al. 2016). Following extraction of FAB, the highly depleted residual harzburgitic mantle remained in the mantle wedge and was fluxed by slab-derived fluids. Boninitic magmas were then generated at low pressure possibly via partial melting of diapirs of slab-metasomatized residual MORB mantle. A similar chemotemporal model has been proposed for the Oman ophiolite (Alabaster et al. 1982) and could be a model for many supra-subduction zone ophiolites as summarized by Whattam and Stern (2011).

The Expedition 352 FAB pre-date boninite formation by no more than 0.6 m.y. (Reagan et al. 2019), which is similar to the rapid time-frame of magma sequences in ophiolites (e.g., Rioux et al. 2012). Results of this study corroborate a similar chemotemporal progression of the Izu-Bonin forearc with subduction initiation ophiolites. This in turn implies similar origins for the IBM forearc and "subduction-initiation rule" (Whattam and Stern 2011) ophiolites. The chemo-temporal transition from FAB to boninite in lavas of both ophiolites and the Izu-Bonin forearc

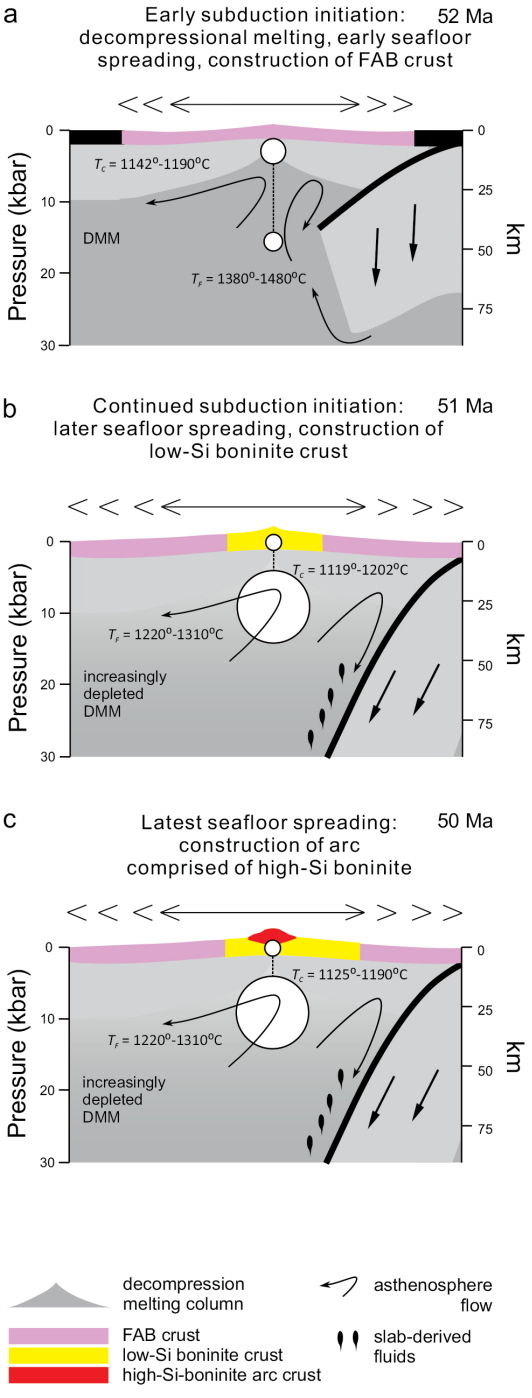

Figure 17. Cartoon depicting the tectonomagmatic evolution (after Reagan et al. 2017) and formation and crystallization histories of the (**a**) FAB and (**b**) boninite. Formation pressure and temperature constraints for the FAB and boninite are from Shervais et al. (2019) and Shervais (in review), respectively. The boninite formation temperature is based on the boninite comprising 3 wt% H_2O. The white circles encompass the range of pressure conditions but because the range of pressure of crystallization of the boninite is small (0.2–0.4 kbar) its circle is enlarged ×5. TF and TC = formation temperature and crystallization temperature (ranges). DMM = depleted MORB mantle. (Color online.)

have been interpreted to reflect a dynamic, tectonic setting with rapidly changing conditions of magma genesis that accompany the deepening of the slab and evolution of slab-derived fluid pathways over the course of subduction initiation (Whattam and Stern 2011; Stern et al. 2012). Such a progression is becoming increasingly apparent for ophiolites (e.g., Shervais 2001; Pearce and Robinson 2010; Whattam and Stern 2011; Stern et al. 2012; Moghadam et al. 2014) and other intra-oceanic forearcs (e.g., Torro et al. 2017; Whattam 2018; Whattam et al. 2020) on a global scale.

Acknowledgments

This research used samples and data provided by the International Ocean Discovery Program (IODP). We thank the crew and scientific staff onboard Expedition 352, particularly Katarina Petronotis, for their excellent work. S.A.W. thanks T. Ishikawa for sharing compositional data of Semail ophiolite boninite minerals. We thank numerous anonymous reviewers whose suggestions greatly improved the manuscript.

Funding

S.A.W. acknowledges support from the Korea International Ocean Discovery Program (K-IODP) funded by the Ministry of Oceans and Fisheries, Korea. We also acknowledge support from NSF award OCE-1558689 (JWS) and OCE-1558688 (MKR). J.S. acknowledges support by the Basic Science Research Program through the National Research Foundation of Korea (NRF) funded by the Ministry of Education (2016R1D1A3B03931481). T.C. acknowledges the Australia-New Zealand IODP consortium (ANZIC), which enabled participation on Exp. 352 and post-expedition funding via the support of government agencies and universities together with the ARC LIEF scheme (LE140100047). H.L. acknowledges support from the National Program on Global Change and Air-Sea Interaction (GASI-GEOGE-02).

References cited

Acland, A.S. (1996) Magma genesis in the northern Lau Basin, SW Pacific. Ph.D. dissertation, Durham University.

Alabaster, T., Pearce, J.A., and Malpas, J. (1982) The volcanic stratigraphy and petrogenesis of the Oman ophiolite complex. Contributions to Mineralogy and Petrology, 81, 168–183.

Arai, S. (1992) Chemistry of chromian spinel in volcanic rocks as a potential guide to magma history. Mineralogical Magazine, 56, 173–184.

Arculus, R.J., Ishizuka, O., Bogus, K.A., Gurnis, M., Hickey-Vargas, R., Aljahdali, M.H., Bandini-Maeder, A.N., Barth, A.P., Brandl, P.A., Drab, L., and others. (2015) A record of spontaneous subduction initiation in the Izu-Bonin-Mariana arca. Nature Geosciences, 8, 728–733.

Ballhaus, C., Berry, R.F., and Green, D.H. (1991) High pressure experimental calibration of the olivine-orthopyroxene-spinel oxygen geobarometer: implications for the oxidation state of the upper mantle. Contributions to Mineralogy and Petrology, 107, 27, https://doi.org/10.1007/BF00311183

Beattie, P. (1993) Olivine-melt and orthopyroxene-melt equilibria. Contributions to Mineralogy and Petrology, 115, 103–111.

Bloomer, S.H., and Hawkins, J.W. (1983) Gabbroic and ultramafic rocks from the Mariana Trench; an island arc ophiolite. In D.E. Hayes, Ed., The Tectonic and Geologic Evolution of Southeast Asian Seas and Islands: Part 2, vol. 27, p. 294–317. Geophysical Monograph Series, AGU, Washington, D.C.

——— (1987) Petrology and geochemistry of boninite series volcanic rocks from the Mariana trench. Contributions to Mineralogy and Petrology, 97, 361–377.

Bloomer, S.H., Taylor, B., MacLeod, C.J., Stern, R.J., Fryer, P., Hawkins, J.W., and Johnson, L. (1995) Early arc volcanism and the ophiolite problem: a perspective from drilling in the western Pacifica. In B. Taylor and J. Natland, Eds., Active Margins and Marginal Basins of the Western Pacifica. Geophysical Monograph, 88, 1–30. http://dx.doi.org/10.1029/GM088p0001

Blundy, J., Cashman, K., and Humphreys, M. (2006) Magma heating by decompression-driven crystallization beneath andesite volcanoes. Nature, 443, 76–80. doi:10.1038/nature05100.

Brounce, M., Kelley, K.A., Cottrell, E., and Reagan, M.J. (2015) Temporal evolution of mantle wedge oxygen fugacity during subduction initiation. Geology, 43, 775–778.

Cameron, W.E. (1985) Petrology and origin of primitive lavas from the Troodos ophiolite, Cyprus. Contributions to Mineralogy and Petrology, 89, 239–255.

Cluzel, D., Aitchison, J.C., and Picard, C. (2001) Tectonic accretion and underplating of mafic terranes in the Late Eocene intraoceanic fore-arc of New Caledonia (Southwest Pacific): Geodynamic implications. Tectonophysics, 340, 23–59.

Coleman, R.G. (1981) Tectonic setting for ophiolite obduction in Oman. Journal of Geophysical Research, 86, 2497–2508.

Crawford, A.J., Falloon, T.J., and Green, D.H. (1989) Classification, petrogenesis and tectonic setting of boninites. In A.J. Crawford, Ed., Boninites and Related Rocks,

pp. 1–49. Unwin Hyman, London,
Danyushevsky, L.V., and Sobolev, A.V. (1996) Ferric-ferrous ratio and oxygen fugacity calculations for primitive mantle-derived melts: Calibration of an empirical technique. Mineralogy and Petrology, 57, 229–241.
Dare, S.A.S., Pearce, J.A., McDonald, I., and Styles, M.T. (2009) Tectonic discrimination of peridotites using f_{O_2}–Cr# and Ga–Ti–Fe^{III} systematics in chrome–spinel. Chemical Geology, 261, 199–216.
DeBari, S.M., Taylor, B., Spencer, K., and Fujioka, K. (1999) A trapped Philippine Sea Plate origin for MORB from the inner slope of the Izu-Bonin Trench. Earth and Planetary Science Letters, 174, 183–197.
Devine, J.D., Rutherford, M.J., Norton, G.E., and Young, S.R. (2003) Magma storage region processes inferred from geochemistry of Fe-Ti oxides in andesitic magma, Soufriere Hills Volcano, Monserrat, WI. Journal of Petrology, 44, 1375–1400.
Dilek, Y., Furnes, H., and Shallo, M. (2007) Suprasubduction zone ophiolite formation along the periphery of Mesozoic Gondwana. Gondwana Research, 11, 453–475.
——— (2008) Geochemistry of the Jurassic Mirdita Ophiolite (Albania) and the MORB to SSZ evolution of a marginal basin oceanic crust. Lithos, 100, 174–209.
Dobson, P.F., and O'Neil, J.R. (1987) Stable isotope compositions and water contents of boninite series volcanic rocks from Chichijima. Bonin Islands, Japan. Earth and Planetary Science Letters, 82, 75–86.
Dobson, P.F., Skogby, H., and Rossman, G.R. (1995) Water in boninite glass and coexisting orthopyroxene: concentration and partitioning. Contributions to Mineralogy and Petrology, 118, 414–419.
Dobson, P.F., Blank, J.G., Maruyama, S., and Liou (2006) Petrology and geochemistry of boninite-series rocks, Chichijima, Bonin Islands, Japan. International Geology Review, 48(8), 669–701. doi: 10.2747/0020-6814.48.8.669.
Droop, G.T.T. (1987) A general equation for estimating Fe^{3+} concentrations in ferromagnesian silicates and oxides from microprobe analyses, using stoichiometric criteria. Mineralogical Magazine, 51, 431–435.
Evans, C.A., Casteneda, G., and Franco, F. (1991) Geochemical complexities preserved in the volcanic rocks of the Zambales ophiolite, Philippines. Journal of Geophysical Research, 96, 16,251–16,262. doi: 10.1029/91JB01488.
Gavrilenko, M., Herzberg, C., Vidito, C., Carr, M.J., Tenner, T., and Ozerov, A. (2018) A calcium-in-olivine geohygrometer and its application to subduction zone magmatism. Journal of Petrology, 57, 1811–1832. doi: 10.1093/petrology/egw062.
Green, D.H. (1973) Experimental melting studies on a model upper mantle composition under water-saturated and water-undersaturated conditions. Earth and Planetary Science Letters, 19, 37–53.
——— (1976) Experimental testing of "equilibrium" partial melting of peridotite under water-saturated, high-pressure conditions. Canadian Mineralogist, 14, 255–268.
Hall, C.E., Gurnis, M., Sdrolias, M., Lavier, L.L., and Müller, D.R. (2003) Catastrophic initiation of subduction following forced convergence across fracture zones. Earth and Planetary Science Letters, 212(1-2), 15–30. http://dx.doi.org/10.1016/S0012-821X(03)00242-5
Hickey-Vargas, R., Yogodzinski, G. M., Ishizuka, O., McCarthy, A., Bizimis, M., Kusano, Y., Savov, I.P., and Arculus, R. (2018) Origin of depleted basalts during subduction initiation and early development of the Izu-Bonin-Mariana Island arc: Evidence from IODP Expedition 351 Site U1438, Amami-Sankaku Basin. Geochimica et Cosmochimica Acta, 229, 85–111. https://doi.org/10.1016/j.gca.2018.03.007
Hoover, J.D., and Irvine, T.N. (1977) Liquidus relationships and Mg-Fe partioning on part of the system $MgSi_2O_4$-Fe_2SiO_4-$CaMgSi_2O_6$-$CaFeSi_2O_6$-$KaAlSi_3O_8$-SiO_2. Carnegie Institute of Washington Yearbook, 77, 774–784.
Ishikawa, T., Nagaishi, K., and Umino, S. (2002) Boninitic volcanism in the Oman ophiolite: Implications for the thermal condition during transition from spreading ridge to arc. Geology, 30, 899–902.
Ishizuka, O., Kimura, J.-I., Li, Y.B., Stern, R.J., Reagan, M.K., Taylor, R.N., Ohara, Y., Bloomer, S.H., Ishii, T., Hargrove, U.S. III, and Haraguchi, S. (2006) Early stages in the evolution of Izu-Bonin arc volcanism: New age, chemical, and isotopic constraints. Earth and Planetary Science Letters, 250(1–2), 385–401. http://dx.doi.org/10.1016/j.epsl.2006.08.007
Ishizuka, O., Tani, K., Reagan, M.K., Kanayama, K., Umino, S., Harigane, Y., Sakamoto, I., Miyajima, Y., Yuasa, M., and Dunkley, D.J. (2011) The timescales of subduction initiation and subsequent evolution of an oceanic island arca. Earth and Planetary Science Letters, 306(3-4), 229–240. http://dx.doi.org/10.1016/j.epsl.2011.04.006.
Jarosewich, E., Nelen, J.A., and Norberg, J.A. (1980) Reference samples for electron microprobe analysis. Geostandards Newsletter, 4, 43–47.
Kamenetsky, V., Crawford, A.J., and Meffre, S. (2001) Factors controlling chemistry of magmatic spinel: An empirical study of associated olivine, Cr-spinel and melt inclusions from primitive rocks. Journal of Petrology, 2, 655–671.
Kodaira, S., Fujiwara, T., Noguchi, N., and Takahashi, N. (2011) Structural variation of the Bonin ridge revealed by modeling of seismic and gravity data. Earth Planets Space, 63, 963–973. doi:10.5047/eps.2011.06.036.
Kushiro, I. (1972) Effect of water on the composition of magmas formed at high pressures. Journal of Petrology, 13, 311–334.
——— (1974) Melting of hydrous upper mantle and possible generation of andesitic magmas: An approach from synthetic systems. Earth and Planetary Science Letters, 22, 294–299.
Kushiro, M.J.A. (2007) Origin of magmas in subduction zones: A review of experimental studies. Proceedings of the Japan Academy, Series B, Physical and Biological Sciences, 83.
Lange, R.A. (1994) The effect of H_2O, CO_2, and F on the density of and viscosity of silicate melts. Reviews of Mineralogy, 30, 331–369.
Lange, R.L., and Carmichael, I.S.E. (1990) Thermodynamic properties of silicate liquids with emphasis on density, thermal expansion and compressibility. Reviews in Mineralogy, 24, 25–64.
LeBas, M.J. (2000) IUGS reclassification of the high-Mg and picritic volcanic rocks. Journal of Petrology, 41(10), 1467–1470.
Lee, C.-T.A., Luffi, P., Plank, T., Dalton, H.A., and Leeman, W.P. (2009) Constraints on the depths and temperatures of basaltic magma generation on Earth and other terrestrial planets. Earth and Planetary Science Letters, 279, 20–33, doi:10.1016/j.epsl.2008.12.020.
Leng, W., and Gurnis, M. (2015) Subduction initiation at relict arcs. Geophysical Research Letters, 42, 7014–7021. doi:10.1002/2015GL064985.
Li, H.Y., Taylor, R.N., Prytulak, J., Kirchenbaur, M., Shervais, J.W., Ryan, J.G., Godard, M., Reagan, M.K., and Pearce, J.A. (2019) Radiogenic isotopes document the start of subduction in the Western Pacific. Earth and Planetary Science Letters, 518, 197–210. https://doi.org/10.1016/j.epsl.2019.04.041.
McDonough, W.F., and Sun, S.S. (1995) The composition of the Earth. Chemical Geology, 120, 223–253.
Metcalf, R.V., and Shervais, J.W. (2008) Suprasubduction-zone ophiolites: Is there really an ophiolite conundrum? The Geological Society of America Special Paper, 408, 191–222. doi: 0.1130/2008.2438(07).
Mitchell, A.L., and Grove, T.L. (2015) Melting the hydrous, subarc mantle: The origin of primitive andesites. Contributions to Mineralogy and Petrology, 170, 13. doi: 10.1007/s00410-015-1161-4.
Miyashiro, A. (1973) The Troodos ophiolitic complex was probably formed in an island arca. Earth and Planetary Science Letters, 19, 218–224.
Moghadam, H.S., and Stern, R.J. (2014) Ophiolites of Iran: Keys to understanding the tectonic evolution of SW Asia: (I) Paleozoic ophiolites. Gondwana Research, 91, 19–38.
Moghadam, H.S., Zaki Khedr, M., Chiaradia, M., Stern, R.J., Bakhshizad, F., Arai, S., Ottley, C.J., and Akihiro, T. (2014) Supra-subduction zone magmatism of the Neyriz ophiolite, Iran: Constraints from geochemistry and Sr-Nd-Pb isotopes. International Geology Review, 56(11), 1395–1412.
Monnier, C., Girardeau, J., Maury, R.C., and Cotten, J. (1995) Back-arc basin origin for the East Sulawesi ophiolite (eastern Indonesia). Geology, 23, 851–854.
Moores, E.M. (1982) Origin and emplacement of ophiolites. Reviews of Geophysics and Space Physics, 20, 735–760.
Morimoto, N. (1988) Nomenclature of pyroxenes. Mineralogical Magazine, 52, 535–550.
Neave, D., and Putirka, K. (2017) A new clinopyroxene-liquid barometer, and implications for magma storage pressures under Icelandic rift zones. American Mineralogist, 102, 777–794.
Niu, Y., O'Hara, M.J., and Pearce, J. (2003) Initiation of subduction zones as a consequence of lateral compositional buoyancy contrast within the lithosphere: A petrological perspective. Journal of Petrology, 44, 851–866. http://dx.doi.org/10.1093/petrology/44.5.851
Ochs, F.A. III, and Lange, R.A. (1999) The density of hydrous magmatic liquids. Science, 283, 1314–1317. doi: 10.1126/science.283.5406.1314.
Macpherson, C.G., and Hall, R. (2001) Tectonic setting of Eocene boninite magmatism in the Izu-Bonin-Mariana forearc. Earth and Planetary Science Letters, 186, 215–230.
Pearce, J.A. (2003) Supra-subduction zone ophiolites: The search for modern analogues. In Y. Dilek and S. Newcomb, Eds., Ophiolite concept and the evolution of geological thought. Geological Society of America Special Paper 373, pp. 269–293.
Pearce, J.A., and Reagan, M.K. (2019) Identification, classification, and interpretation of boninites from Anthropocene to Eoarchean using Si-Mg-Ti systematics. Geosphere, 15, https://doi.org/10.1130/GES01661.1
Pearce, J.A., and Robinson, P.T. (2010) The Troodos ophiolitic complex probably formed in a subduction initation, slab edge setting. Gondwana Research, 18(1), 60–81. doi:10.1016/j.gr.2009.12.003.
Pearce, J.A., Lann, S.R., Arculus, R.J., Murton, B.J., Ishii, T., Peate, D.W., and Parkinson, I.J. (1992) Boninite and harzburgite from Leg 125 (Bonin-Mariana fore-arc): A case study of magma genesis during the initial stages of subduction. In P. Fryer, J.A. Peace, and L.B. Stokking, Eds., Proceedings of the Ocean Drilling Program, Scientific Results, 125, p. 623–659. Ocean Drilling Program, College Station, Texas.
Pearce, J.A., Barker, P.F., Edwards, S.J., Parkinson, I.J., and Leat, P.T. (2000) Geochemistry and tectonic significance of peridotites from the South Sandwich arc-basin system, South Atlantica. Contributions to Mineralogy and Petrology, 139, 36–53.
Portnyagin, M.V., Danyushevsky, L.V., and Kamenetsky, V.S. (1997) Coexistence of two distinct mantle sources during formation of ophiolites: A case study of primitive pilliow-lavas from the lowest part of the volcanic section of the Troodos Ophiolite, Cyprus. Contributions to Mineralogy and Petrology, 128, 287–301.
Putirka, K. (1999) Clinopyroxene + liquid equilibria to 100 kbar and 2450 K. Contributions to Mineralogy and Petrology, 135, 151–163.
Putirka, K.D. (2008) Thermometers and barometers for volcanic systems. Reviews of Mineralogy and Geochemistry, 69, 61–120.
Putirka, K., Johnson, M., Kinzler, R., and Walker, D. (1996) Thermobarometry of mafic igneous rocks based on clinopyroxene-liquid equilibria, 0–30 kbar. Contributions to Mineralogy and Petrology, 123, 92–108.

Putirka, K., Mikaelian, H., Ryerson, F.J., and Shaw, H. (2003) New igneous thermobarometers for mafic and evolved lava compositions, based on clinopyroxene + liquid equilibria. American Mineralogist, 88, 1542–1554.
Reagan, M.K., Ishizuka, O., Stern, R.J., Kelley, K.A., Ohara, Y., Blichert-Toft, J., Bloomer, S.H., Cash, J., Fryer, P., Hanan, B.B., and others. (2010) Fore-arc basalts and subduction initiation in the Izu-Bonin-Mariana system. Geochemistry, Geophysics, Geosystems 11, Q03X12, doi:10.1029/2009GC002871.
Reagan, M.K., McClelland, W.C., Girard, G., Goff, K.R., Peate, D.W., Ohara, Y., and Stern, R.J. (2013) The geology of the southern Mariana fore-arc crust: implications for the scale of Eocene volcanism in the western Pacifica. Earth and Planetary Science Letters, 380, 41–51. http://dx.doi.org/10.1016/j.epsl.2013.08.013
Reagan, M.K., Pearce, J.A., Petronotis, K., and the Expedition 352 Scientists (2015) Izu-Bonin-Mariana Fore Arca. Proceedings of the International Ocean Discovery Program, 352: College Station, Texas (International Ocean Discovery Program), http://dx.doi.org/10.14379/ iodp.proc.352.2015
Reagan, M.K., Pearce, J.A., Petronotis, K., Almeev, R.R., Avery, A.J., Carvallo, C., Chapman, T., Christeson, G.L., Ferré, E.C., Godard, M., and others. (2017) Subduction initiation and ophiolite crust: New insights from IODP drilling. International Geology Review, 59, 1439–1450. http://dx.doi.org/10.1080/00206814.2016.1276482
Reagan, M.K., Heaton, D.E., Schmizt, M.D., Pearce, J.A., Shervais, J.W., and Koppers, A.P (2019) Forearc ages reveal extensive short-lived and rapid seafloor spreading following subduction initiation. Earth and Planetary Science Letters, 506, 520–529. https://doi.org/10.1016/j.epsl.2018.11.020
Rhodes, J.M., Lofgren, G.E., and Smith, B.P. (1979) One atmosphere melting experiments on ilmenite basalt 12 000. Proceedings of the 10th Lunar Science Conference, pp. 407–422.
Rioux, M., Bowring, S., Kelemen, P., Gordon, S., Dudás, F., and Miller, R. (2012) Rapid crustal accretion and magma assimilation in the Oman-U.A.E. ophiolite: High precision U-Pb zircon geochronology of the gabbroic crust. Journal of Geophysical Research: Solid Earth, 117, B7. doi:10.1029/2012JB009273.
Roeder, P.L., and Emslie, R.F. (1970) Olivine-liquid equilibrium. Contributions to Mineralogy and Petrolrolgy, 29, 275–289, https://doi.org/10.1007/BF00371276
Saccani, E., and Photiades, A. (2004) Mid-ocean ridge and supra-subduction affinities in the Pindos Massif ophiolites (Greece): Implications for magma genesis in a proto-forearc setting. Lithos, 73, 229–253.
Saccani, E., Bortolotti, V., Marroni, M., Pandolfi, L., Photiades, A., and Principi, G. (2008) The Jurassic association of backarc basin ophiolites and calk-alkaline volcanics in the Guevgueli Complex (northern Greece): Implication for the evolution of the Vardar Zone. Ophioliti, 33, 209–227.
Sato, H. (1977) Nickel content of basaltic magmas: Identification of primary magmas and a measure of the degree of olivine fractionation. Lithos, 10, 113–120.
Scruggs, M.A. and Putirka, K.D. (2018) Eruption triggering by partial crystallization of mafic enclaves at Chaos Crags, Lassen Volcanic Center, California. American Mineralogist, 103, 1575–1590. https://doi.org/10.2138/am-2018-6058.
Shervais, J.W. (2001) Birth, death and resurrection: The life cycle of supra-subduction zone ophiolites. Geochemistry, Geophysics, Geosystems, 2, 2000GC000080.
Shervais, J.W., Reagan, M., Haugen, E., Almeev, R., Pearce, J., Prytulak, J., Ryan, J.G., Whattam, S.A., Godard, M., Chapman, T., and others. (2019) Magmatic response to subduction initiation, Part I: Fore-arc basalts of the Izu-Bonin Arc from IODP Expedition 352. Geochemistry, Geophysics, Geosystems, 20/1, 314–338, Article GGGE21778. doi: 10.1029/2018GC007731.
Sobolev, A.V., and Danyushevsky, L.V. (1994) Petrology and geochemistry of boninites from the north termination of the Tonga Trench: Constrains on the generation conditions of primary high-Ca boninite magmas. Journal of Petrology, 35, 1183–1211.
Stern, R.J., and Bloomer, S.H. (1992) Subduction zone infancy: Examples from the Eocene Izu-Bonin-Mariana and Jurassic California. Geological Society of America Bulletin, 104, 1621–1636.
Stern, R.J., Reagan, M., Ishizuka, O., Ohara, Y., and Whattam, S. (2012) To understand subduction initiation, study forearc crust; to understand forearc crust, study ophiolites. Lithosphere, 4, 469–483.
Straub, S.M., LaGatta, A.B., Martin-Del Pozzo, A.L., and Langmuir, C.H. (2008) Evidence from high-Ni olivines for a hybridized peridotite/pyroxenite source for orogenic andesites from the central Mexican Volcanic Belt. Geochemistry, Geophysics, Geosystems, 9, doi.10.1029/2007GC001583.
Takahashi, E., Uto, K., and Schilling, J.G. (1987) Primary magma compositions and Mg/Fe ratios of the mantle residues along Mid Atlantic Ridge 29°N to 73°N. Technical Reports of ISEI, Okayama University, A9, pp. 1–14.
Tanaka, H.K.M., Kusagaya, T., and Shinohara, H. (2014) Radiographic visualization of magma dynamics in an erupting volcano. Nature Communications, 5, 3381. doi: 10.1038/ncomms4381.
Tatsumi, Y., and Maruyama, S. (1989) Boninites and high-Mg andesites: Tectonics and petrogenesis. In A.J. Crawford, Ed., Boninites and Related Rocks, pp. 50–71. Unwin and Hyman.
Taylor, R.N., Nesbitt, R.W., Vidal, P., Harmon, R.S., Auvray, B., and Croudace, I.W. (1994) Mineralogy, chemistry, and genesis of the boninite series volcanics, Chichijima, Bonin Islands, Japan. Journal of Petrology, 35(3), 577–617.
Thompson, G.M., Malpas, J., and Smith, I.E.M. (1997) The geochemistry of tholeiitic and alkalic plutonic rocks within the Northland ophiolite, northern New Zealand: Magmatism in a back arc basin. Chemical Geology, 142, 213–223.
Topliss, M.J., and Carroll, M.R. (1995) An experimental study of the influence of oxygen fugacity on Fe-Ti oxide stability, phase relations and mineral-melt equilibria in ferro-basaltic systems. Journal of Petrology, 36, 1137–1170.
Torró, L., Proenza, J.A., Marchesi, C., Garcia-Casco, A., and Lewis, J.F. (2017) Petrogenesis of meta-volcanic rocks from the Maimón Formation (Dominican Republic): Geochemical record of the nascent Greater Antilles paleo-arc. Lithos, 278-281, 255–273. http://dx.doi.org/10.1016/j.lithos.2017.01.031
Ulmer, P. (1989) The dependence of the Fe^{2+}-Mg cation-partitioning between olivine and basaltic liquid on pressure, temperature and composition, an experimental study to 30 kbars. Contributions to Mineralogy and Petrology, 101, 261–273.
Umino, S. (1986) Magma mixing in boninite sequence of Chichijima, Bonin Islands. Journal of Volcanology and Geothermal Research, 29, 125–157.
Umino, S., and Kushiro, I. (1989) Experimental studies on boninite petrogenesis. In A.J. Crawford, Ed., Boninite and Related Rocks, pp. 89–109. Unwin Hyman.
van der Laan, S.R., Flower, M.F.J., Koster Van Groos, A.K. (1989) Experimental evidence for the origin of boninites: near-liquidus phase relations to 7.5 kbar. In A.J. Crawford, Ed., Boninite and Related Rocks, pp. 112–147. Unwin Hyman.
van der Laan, S.R., Arculus, R.J., Pearce, J.A., and Murton, B.J. (1992) Petrography, mineral chemistry, and phase relations of the basement boninite series of Site 786, Izu-Bonin forearca. In P. Fryer, J.A. Pearce, et al., Eds., Proceedings of the Ocean Drilling Program, Scientific results, vol. 125, p. 171–201. Ocean Drilling Program, College Station, Texas.
Venezsky, D.Y., and Rutherford, M.J. (1999) Petrology and Fe-Ti oxide reequilibration of the 1991 Mount Unzen mixed magma. Journal of Volcanology and Geothermal Research, 89, 213–230.
Whattam, S.A. (2009) Arc-continent collisional orogenesis in the SW Pacific and the nature, source and correlation of emplaced ophiolitic nappe components. Lithos, 113, 88–114.
——— (2018) Primitive magmas in the early Central American Arc system generated by plume-induced subduction initiation. Frontiers in Earth Science, 6, 114. doi: 10.3389/feart.2018.00114.
Whattam, S.A., and Stern, R.J. (2011) The "subduction initation rule": A key for linking ophiolites, intra-oceanic arcs and subduction initiation. Contributions to Mineralogy and Petrology, 162, 1031–1045. doi: 10.1007/s00410-011-0638-z.
Whattam, S.A., Montes, C., and Stern, R.J. (2020) Early Central American forearc follows the subduction initiation rule. Gondwana Research, 79, 283–300. https://doi.org/10.1016/j.gr.2019.10.002.
Wu, J., Suppe, J., and Kanda, R. (2016) Philippine Sea and East Asian plate tectonics since 52 Ma constrained by new subducted slab reconstruction methods. Journal of Geophysical Research, 121, 4670–4741. doi: 10.1002/2016JB012923.
Yajima, K., and Fujimaki, H. (2001) High-Ca and low-Ca boninites from Chichijima, Bonin (Ogasawara) archipelago. Japanese Magazine of Mineralogical and Petrological Sciences, 30, 217–236.
Yogodzinski, G.M., Bizimis, M., Hickey-Vargas, R., McCarthy, A., Hocking, B.D., Savov, I.P., et al. (2018). Implications of Eocene-age Philippine Sea and forearc basalts for initiation and early history of the Izu-Bonin-Mariana arca. Geochimica et Cosmochimica Acta, 228, 136–156. https://doi.org/10.1016/j.gca.2018.02.047

Manuscript received May 17, 2018
Manuscript accepted March 7, 2020
Manuscript handled by Susanne Straub

Endnote:

[1]Deposit item AM-20-106640, Supplemental Material. Deposit items are free to all readers and found on the MSA website, via the specific issue's Table of Contents (go to http://www.minsocam.org/MSA/AmMin/TOC/2020/Oct2020_data/Oct2020_data.html).